

AD 742334

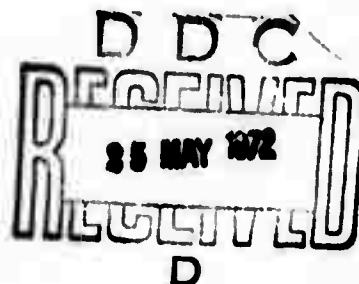
NRL Report 7445

Optical Analysis for the 1971 ARPA Tower Experiment

DENZIL STILWELL, JR.

*Electromagnetic Scattering Branch
Electronics Division*

May 12, 1972



Reproduced by
**NATIONAL TECHNICAL
INFORMATION SERVICE**
Springfield, Va. 22151

NAVAL RESEARCH LABORATORY
Washington, D.C.

Approved for public release; distribution unlimited.

R 54

DOCUMENT CONTROL DATA - R & D

(Security classification of title, body of abstract and indexing annotation must be entered when the overall report is classified)

1. ORIGINATING ACTIVITY (Corporate author)		2a. REPORT SECURITY CLASSIFICATION	
Naval Research Laboratory Washington, D.C. 20390		Unclassified	
3. REPORT TITLE		2b. GROUP	
OPTICAL ANALYSIS FOR THE 1971 ARPA TOWER EXPERIMENT			
4. DESCRIPTIVE NOTES (Type of report and inclusive dates)			
Final report on the NRL Problem.			
5. AUTHOR (First name, middle initial, last name)			
Denzil Stilwell, Jr.			
6. REPORT DATE	7a. TOTAL NO. OF PAGES	7b. NO. OF REFS	
May 12, 1972	58	4	
8a. CONTRACT OR GRANT NO.	9a. ORIGINATOR'S REPORT NUMBER(S)		
NRL Problem: R07-02	NRL Report 7445		
b. PROJECT NO.	9b. OTHER REPORT NO(S) (Any other numbers that may be assigned this report)		
Project 1E20 ARPA No. 1907			
d.			
10. DISTRIBUTION STATEMENT			
Approved for public release; distribution unlimited.			
11. SUPPLEMENTARY NOTES		12. SPONSORING MILITARY ACTIVITY	
		Advanced Research Projects Agency Arlington, Virginia 22209	
13. ABSTRACT			
<p>During the months of September and October 1971, the Naval Research Laboratory performed optical measurements at the Naval Undersea Research and Development Center tower off Mission Bay near San Diego, California. The optical measurements consisted of oblique photographs and wide-angle photography from which the ocean spectrum was analyzed as a function of time using the Sea Photo Analysis (SPA) technique. In conjunction with measurements being made simultaneously by other investigators, an attempt was made to experimentally determine the interaction of internal waves and wind-driven surface waves. This report discusses the results of the optical analysis of the sea photographs taken at 15-s intervals. The results show temporal variations of the spectral amplitude in the range of wavelengths from about 3 cm to 1 m. These temporal variations exhibit changes as large as 15 dB on occasion. Because of the superposition of many effects, such as tides, magnitude and direction variations of the wind, internal-wave amplitude, contamination; no unique signature was deduced for the interaction of internal and surface waves. There is evidence for a mild frequency dependence of the interaction.</p>			

14 KEY WORDS	LINK A		LINK B		LINK C	
	ROLE	WT	ROLE	WT	ROLE	WT
Sea photo analysis (SPA) Optical analysis Spectral analysis Fourier spectrum Two-dimensional wavenumber spectra Wave visibility Directional waveheight spectra Internal-wave/surface-wave interaction Stationarity Homogeneity Internal waves Oblique photography Slicks						

CONTENTS

Abstract	ii
Problem Status	ii
Authorization	ii
INTRODUCTION	1
COORDINATE SYSTEM	1
WAVE VISIBILITY IN TWO DIMENSIONS	3
SUBRESOLUTION WAVES	5
OPTICAL ANALYSIS	6
PHOTOGRAPHIC SPECTRUM	6
DIRECTIONAL DISTORTION	8
OCEAN SPECTRUM	9
LONG-WAVELENGTH SPECTRUM	10
SLOPE, WAVEHEIGHT, AND FREQUENCY SPECTRA	11
EMPIRICAL SPECTRA	12
TRANSIENT STATES: STATIONARITY AND HOMOGENEITY	13
TOWER INSTALLATION	13
DATA ANALYSIS	15
EXPERIMENTAL RESULTS	16
CONCLUSIONS	53
REFERENCES	54

ABSTRACT

During the months of September and October 1971, the Naval Research Laboratory performed optical measurements at the Naval Undersea Research and Development Center tower off Mission Bay near San Diego, California. The optical measurements consisted of oblique photographs and wide-angle photography from which the ocean spectrum was analyzed as a function of time using the Sea Photo Analysis (SPA) technique. In conjunction with measurements being made simultaneously by other investigators, an attempt was made to experimentally determine the interaction of internal waves and wind-driven surface waves. This report discusses the results of the optical analysis of the sea photographs taken at 15-s intervals. The results show temporal variations of the spectral amplitude in the range of wavelengths from about 3 cm to 1 m. These temporal variations exhibit changes as large as 15 dB on occasion. Because of the superposition of many effects, such as tides, magnitude and direction variations of the wind, internal-wave amplitude, contamination; no unique signature was deduced for the interaction of internal and surface waves. There is evidence for a mild frequency dependence of the interaction.

PROBLEM STATUS

A final report on the NRL Problem.

AUTHORIZATION

NRL Problem R07-02
Project 1E20 ARPA No. 1907

Manuscript submitted April 27, 1972.

OPTICAL ANALYSIS FOR THE 1971 ARPA TOWER EXPERIMENT

INTRODUCTION

At moderate wind velocities, the sea surface appears to the eye as a randomly occurring pattern of surface perturbations of never ending variability. Therefore, it is evident that statistical measures are necessary to describe it. Since a point-function description would have a probability of occurrence of zero, it would be analytically monstrous. Fortunately, the conceptually simple, Fourier decomposition of the two-dimensional surface results in fairly simple spectral trends and is very informative. With the advent of Sea Photograph Analysis (SPA), the fundamental functional, the two-dimensional slope, or the tilt-angle spectra has become an observable. Recently, a need for such a representation has arisen to assist ARPA in the analysis of the coupling of surface-wave phenomena with the passage of internal waves. In the past year, the Naval Research Laboratory (Electromagnetic Scattering Branch (Code 5270), Electronics Division) has assisted in the overall ARPA program by determining *in situ* the behavior in the presence of internal waves of that portion of the ocean-wave spectrum lying between 1 m and 3 cm.

The method used, sea photograph analysis, uses oblique photographs of the sea surface to establish the directional spectrum in the "high"-frequency portion of the ocean energy spectrum. This is possible, since under reasonably generalized conditions a single photograph of the ocean surface contains sufficient information from which to deduce the directional distribution of constituent sinusoids which make up the highly complex ocean surface. Such statistical information is of prime importance in any evaluation of the mechanisms of wave-wave interactions or electromagnetic scatter from the sea. This report will update the theoretical bases and experimental techniques which combine to provide remote access to many of the statistical properties of the ocean-surface perturbations, including the time-dependent spectral variations which are necessary in studying internal-wave/surface-wave interaction.

COORDINATE SYSTEMS

To study the features of the ocean surface of importance to optical analysis, it is first necessary to assign a system of coordinates. Figures 1 and 2 illustrate the coordinate system chosen for this analysis. The rationale in choosing the partition into a local coordinate system and one locating the localized point in relation to the sensor is largely the simplicity involved. In general the technique will use the local system to determine the parameters dealing with the properties of a point on the surface of the water and the larger system to describe the variation expected throughout the field of view of the camera.

Figure 1 illustrates the local coordinate system. Here \mathbf{C} represents the unit vector from the point under consideration toward the camera, intersecting the optical axis of the camera at the center of the lens, \mathbf{N} represents the normal to the water at the surface point, and \mathbf{S} is the vector toward the sky in the direction of specular reflection. The

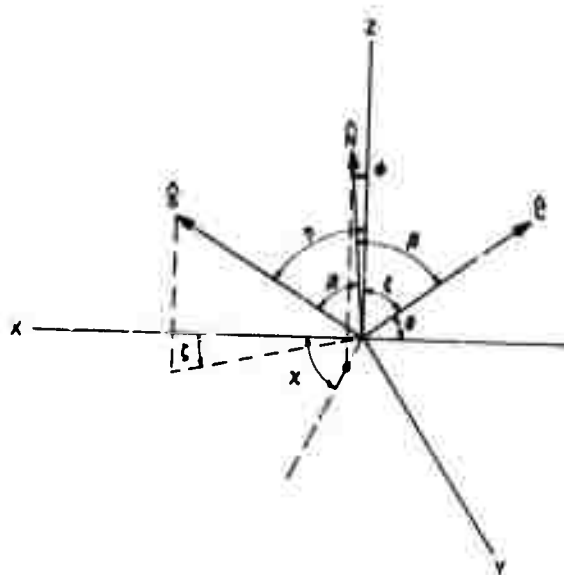


Fig. 1 — Local coordinate system

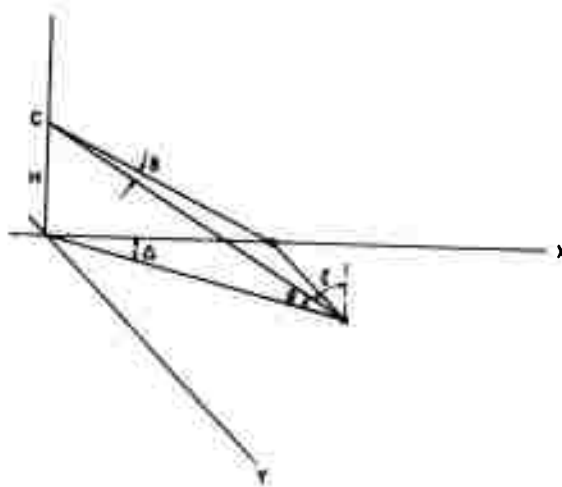


Fig. 2 — Camera coordinate system

local cartesian system referring to the same surface point is labeled XYZ. The angle ψ is between X and the projection of N onto the XY plane. For a sinusoidal surface disturbance, ψ is constant. The angle of incidence of the sky ray with respect to the surface normal is β . The depression angle θ of the surface point from the camera is measured relative to the horizontal plane; ξ is the complement of θ . The angle ϕ is the tilt angle of the surface normal from the zenith and essentially is related to the slope of the surface at a point. The angle η is the normal spherical angle relating the zenith to the sky ray. Finally, ζ is the angle between the X axis and the projection of the sky ray onto the XY plane.

Figure 2 illustrates the camera coordinate system (the angles δ and θ are the basic quantities used in describing points on the film). Here δ is the angle between the ray to the surface point and the ray to the nearest point falling on the projection of the optic axis onto the XY plane. Also Δ is the angle obtained by projecting δ onto the XY plane and is therefore the angle connected with the cardinal directions (north, east, south, and west).

WAVE VISIBILITY IN TWO DIMENSIONS

One of the most important aspects of SPA is wave visibility. From the onset, simple observations convince one that surface waves are most visible at oblique incidence. Further, the usefulness of a horizontally polarizing filter is also apparent. Beyond this it is a difficult mathematical exercise to obtain a unique and quantitative measurement of any but the most simple wave patterns. The full analysis of the intensity of light arriving at an observer at some height above a water surface is almost intractable for the two spatial dimensions and a dimension of light intensity. Fortunately, many of the salient features can be understood from the simpler case which excludes the lateral spatial dimension. The extension to the full situation should reveal little more science and with the present choice of coordinate systems presents no real experimental difficulty. For the purposes of this theoretical discussion, only the two-dimensional case will be considered. In Fig. 2 the light reaching a camera at C from the ocean surface consists of three components: that reflected from the sky, that upwelling component which is scattered from beneath the surface, and that contributed by the media between the camera and the surface point under consideration. Functionally,

$$u \propto \Gamma L + T\ell + s \quad (1)$$

where u is the light energy density, Γ is the reflection coefficient, L is the sky luminance, T is the transmission coefficient, ℓ is the upwelling luminance, and s is the media scattering function. More explicitly,

$$\frac{1}{C} u(\xi, \phi) = \Gamma(\xi + \phi) L(\xi + 2\phi) + T(\xi + \phi) \ell(F(\xi + \phi) + \phi) + s(\xi) \quad (2)$$

in the XZ plane, where F is the refraction function.

An ocean surface for which a spectrum can be accurately defined consists of a smooth variation of the normal angle ϕ for adjacent points at the air-sea boundary. Mathematically speaking, a spectrum is undefined at wind speeds beyond the onset of whitecapping because the surface normal angle becomes multivalued. Realistically, the utility of an ocean-surface spectrum diminishes with increasing whitecap coverage for the high-frequency range, but

the white water can fail to seriously affect spectral estimates in the range of wavelengths containing most of the wave energy until a very significant fraction of the surface is obscured by the whitecaps. With the present state of the art, it is probably impossible to get good photographs in such cases anyway.

An examination of Eq. (2) and its partial derivatives shows that highly discontinuous luminance functions yield maximum contrast (ϕ variation of u) at the cost of overemphasizing the dependence of u on particular values of ϕ and underemphasizing the existence of other slopes. This is observed with sun glitter and is of use in establishing slope distributions but is of little value in ascertaining waveheight distributions. This restriction to smooth and monotonic luminance function is partially removed if it is possible to ignore the very high portion of the wave-number spectrum. (See the section on subresolution waves.)

The light scattering s from the intervening medium represents a major limitation to sea photo analysis. It degrades the transmission of the information inalterably and in the case of clouds may limit the altitude from which it is possible to see the ocean. Such scattering is generally a function of depression angle because of the different distances light must travel to reach the camera from points on the surface. Unfortunately, s is not a uniform function of angle because of atmospheric turbulence and nonhomogeneous particulate distributions; further, it may be a rapid function of time. This accounts for the experimental "fact" that for high angular resolution in camera systems, the resulting imagery always seems degraded over that which would be calculated from the system characteristics or even lower altitude photos of the same wave system.

In many cases of interest, however, it is possible to expand the luminance functions in a power series in ξ or ϕ and retain only low-order terms. With this assumption, the set of equations

$$\frac{1}{C} u_0 = \Gamma_0 L_0 + T_0 \ell_0 + s_0, \quad (3a)$$

$$\frac{1}{C} u_1 = \Gamma_1 L_0 + \Gamma_0 L_1 + T_1 \ell_0 + T_0 \ell_1 + s_1, \quad (3b)$$

$$\vdots$$

and

$$\frac{1}{C} u_n = \sum_{q=0}^{q=n} (\Gamma_q L_{n-q} + T_q \ell_{n-q}) + s_n, \quad (3n)$$

where all the functions u , Γ , L , T , ℓ , and s are considered to have the form

$$u = u_0 + u_1(\xi - \xi_0) + \cdots + u_n(\xi - \xi_0)^n, \quad (4)$$

make it possible to determine L and ℓ . The measurement of u and knowledge of the reflection and transmission coefficients is sufficient, provided the contributions from s are minimal.

It is now possible to compute the "sensitivity," i.e., wave contrast that will exist on a photograph of a wave system. The derivative u_ϕ is taken to express the sensitivity to variations of wave normal angle. Then

$$C^{-1} u_\phi = \Gamma' L + 2\Gamma L' + T'\ell + T\ell'(1 + F'), \quad (5)$$

where the prime represents derivatives with respect to the argument. In addition,

$$C^{-1} u_\xi = \Gamma' L + \Gamma L' + T'\ell + T\ell' F' + s_\xi; \quad (6)$$

then

$$C^{-1} u_\phi = C^{-1} u_\xi + \Gamma L' + T\ell' - s_\xi. \quad (7)$$

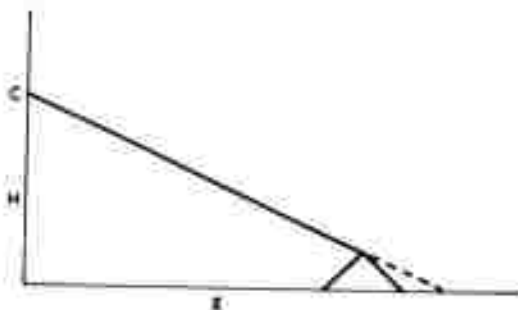
Thus knowledge of $u = u(\xi)$ and of expressions for L' and ℓ' allows the evaluation of the sensitivity to wave variations, again with $s = 0$. Perhaps a more useful form of Eq. (7) is

$$\frac{d}{d\phi} (\ln u) = \frac{d}{d\xi} (\ln u) + \frac{\Gamma L' + T\ell' - s_\xi}{C^{-1} u}. \quad (8)$$

SUBRESOLUTION WAVES

Waves on the ocean surface at a scale smaller than the resolution allowed by camera-film-air turbidity effects can introduce errors in the determination of L and ℓ . To illustrate this, one may consider Fig. 3. The triangular structure, when viewed at this or more shallow angles, causes shadowing. Even at steeper angles there is still a shortening of the nearly shadowed leg. Obviously, water-wave slopes which present a broadside aspect weigh more heavily on the surface brightness than do slopes tilted away from the observer and partially shadowed (projecting smaller areas in the camera direction). Thus three effects arise. The first causes a distortion of any sinusoid, even resolved ones. The second introduces a bias in the apparent distribution of normal angles; this bias is a function of both the depression angle and the unresolved slope distribution. (This will lead to an error in the computation of L and ℓ and thereby affect the measured spectrum.) The third effect is beneficial in that it may extend the utility of SPA. On days for which the sky does not exhibit a "domed" variation of light intensity, e.g., have partially broken clouds, the subresolution waves will tend to smooth the apparent sky variations. Small waves tend to cover the surface uniformly, and consequently the apparent brightness of some point on a long wave is smeared over the sky. Although this may tend to wash out the wave visibility, it can also tend to remove discontinuities in the sky brightness.

Fig. 3 — Perspective distortion resulting from the oblique incidence angle of the camera



It is necessary to use an iterative procedure to determine L and ℓ . This involves obtaining a first estimate of L and ℓ and then computing the spectrum. The effective surface tilt for the subresolution waves is then estimated, and new values of L and ℓ are obtained. The process is continued until the induced tilt is not affected by the iteration. This effect should result in second-order errors in the wave sensitivity equation and can usually be ignored.

OPTICAL ANALYSIS

The optical analysis uses the relationship between light amplitudes in the two focal planes of a lens. A lens has a transfer function between these planes which becomes a pure Fourier transform when used with collimated, monochromatic light. When a positive transparency of a scene is inserted into the collimated beam, an image is reconstructed (just after the transparency) which to within the camera-film limitations is exactly that which existed at the camera due to the scene. In water-wave photography, the small amplitudes of the waves (an inherent characteristic of water waves in the gravity range) provide a linear relation between amplitudes and the surface normal angle. Therefore the light amplitude distribution in the other focal plane is the Fourier transform of the surface-normal-angle variations, and the light intensity is proportional to the energy spectrum of the water waves.

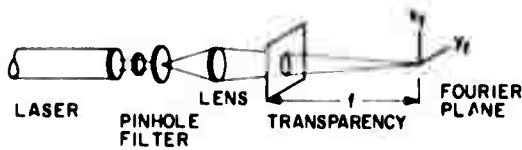


Fig. 4 — Optical analysis system

Figure 4 is a sketch of the usual optical system. This system does not use collimated laser beam because of the extra lenses required and the little benefit it serves. Instead the lens images the spatial-filter pinhole at the Fourier plane; the effective focal length for the transform is just the distance from the transparency to the Fourier plane. This allows the arraignment to have more versatility in that differing illumination areas and effective focal lengths can be generated simply by moving the transparency relative to the lens.

PHOTOGRAPHIC SPECTRUM

Goodman (1) writes that

$$I_f(x_f, y_f) = \frac{A^2}{\lambda^2 f^2} \left| \int_{-\infty}^{\infty} \int_{-\infty}^{\infty} t(x, y) \exp \left[-j \frac{2\pi}{\lambda f} (xx_f + yy_f) \right] dx dy \right|^2 \quad (9)$$

in which $t(x, y)$ is the amplitude transmittance function of the scene for a uniform distribution of amplitude A , λ is the optical wavelength, f is the focal length, x and y are the distances in the scene plane, and x_f and y_f are the distances in the Fourier plane. The integral is equivalent to a Fourier transform.

For SPA the transmittance function associated with the film is

$$t(x, y) = \left[1 + \frac{1}{2} \frac{u_\phi}{u_0} \phi(x, y) \right] t_0. \quad (10)$$

The laser beam is not a uniform distribution but has a Gaussian intensity distribution, so the weighted amplitude transmitted becomes

$$At(x, y) = A_0 t_0 \left[1 + \frac{1}{2} \frac{u_\phi}{u_0} \phi(x, y) \right] \exp \left[-\frac{x^2 + y^2}{\sigma^2} \right]. \quad (11)$$

Consequently

$$I_f = \left(\frac{A_0 t_0}{\lambda f} \right)^2 \left| \mathfrak{F} \left\{ e^{-(x^2 + y^2)/\sigma^2} \right\} + \frac{1}{2} \frac{u_\phi}{u_0} \mathfrak{F} \left\{ \phi(x, y) e^{-(x^2 + y^2)/\sigma^2} \right\} \right|^2, \quad (12)$$

where \mathfrak{F} denotes a Fourier transform. The second term in Eq. (12) reduces to a convolution of the spectra, which produces a smoothing of the ϕ spectrum. Using the Fourier-transform identities

$$F(s) = \int_{-\infty}^{\infty} f(x) e^{-i2\pi xs} dx, \quad (13a)$$

$$f(x) = \int_{-\infty}^{\infty} F(s) e^{i2\pi xs} ds, \quad (13b)$$

$$\mathfrak{F} \{ f(ax) \} = \frac{1}{|a|} F\left(\frac{s}{a}\right), \quad (13c)$$

and

$$\mathfrak{F} \{ e^{-\pi x^2} \} = e^{-\pi s^2}, \quad (13d)$$

we arrive at an explicit form of Eq. (12):

$$I = \left(\frac{A_0 t_0}{\lambda f} \right)^2 \left[|G|^2 + \frac{u_\phi}{u_0} G(G * \bar{\phi}) + \left(\frac{1}{2} \frac{u_\phi}{u_0} \right)^2 |G * \bar{\phi}|^2 \right], \quad (14)$$

where

$$\mathfrak{F} \{ e^{-(x^2 + y^2)/\sigma^2} \} = \pi \sigma^2 \exp \left[-\frac{\pi^2 \sigma^2}{\lambda^2 f^2} (x_f^2 + y_f^2) \right] = G, \quad (15a)$$

$$\mathfrak{F} \{ \phi(x, y) \} = \bar{\phi}, \quad (15b)$$

and the symbol $*$ denotes a convolution.

The middle term of Eq. (14) is weighted so heavily by the Gaussian term that it is to be ignored, as one does the first term, outside a region surrounding the origin. The information is suppressed near the origin due to the strongly peaked Gaussian function.

This can be looked on as a physical manifestation of sampling theory, i.e., the under-sampled wavelengths are obscured by the dc term. Then

$$\{k_x, k_y\} = 2\pi \left\{ \frac{x_f}{\lambda f}, \frac{y_f}{\lambda f} \right\}, \quad (16)$$

where G^2 is the dc term and k_x and k_y refer to film wavenumbers, and letting

$$I_0 = \left(\frac{A_0 t_0}{\lambda f} \pi \sigma^2 \right)^2, \quad (17)$$

one obtains

$$\bar{\phi} \approx 4\pi^2 \sigma^4 \frac{u_0^2}{u_\phi^2} \frac{I}{I_0} = \bar{\phi} * G. \quad (18)$$

The energy spectrum is related to the square of the Fourier transform $\bar{\phi}^2$ by

$$\Phi = \int_k^{k+\Delta k} |\bar{\phi}(k)|^2 dk \quad (19)$$

then

$$\Phi = \frac{4\pi^2 \sigma^4}{I_0} \frac{u_0^2}{u_\phi^2} \int_k^{k+\Delta k} I dk. \quad (20)$$

The intensity in the Fourier-transform plane is constant over a region inversely related to the effective aperture $2\sqrt{2} \sigma$ of the Gaussian illumination in the scene plane. Then

$$\Delta k_x = \Delta k_y = \frac{2\pi}{2\sqrt{2} \sigma}. \quad (21)$$

For the circular region,

$$\pi \left(\frac{\Delta k}{2} \right)^2 = \frac{\pi^3}{2\sigma^2}, \quad (22)$$

and

$$\Phi = \frac{2\pi^5}{I_0} \sigma^2 \frac{u_0^2}{u_\phi^2} I. \quad (23)$$

Equation (23) is valid for the region outside the origin. All the quantities are measurable, and the photographic spectrum is an observable.

DIRECTIONAL DISTORTION

The mapping from real space to film space induces a distortion, due to the obliquity. Thus letting M represent a mapping operator, one has

$$M \phi(X, Y) \rightarrow t(x, y) \quad (24)$$

where

$$k_x = \frac{D}{F} K_X \csc \theta, \text{ and } k_y = \frac{D}{F} K_Y$$

where D is the distance from the camera to the surface point and F is the focal length of the camera. As a result, the photographic transform will exhibit a more restricted directional distribution than that actually existing on the ocean surface.

The effect of oblique perspective only complicates the problem of obtaining the full directional spectra. To determine the angle Ω in the photo spectrum related to a wave on the ocean at a direction ψ , consider

$$\mathbf{K} = i \cos \psi + j \sin \psi \quad (25a)$$

$$\mathbf{k} = \left(i \frac{\cos \psi}{\sin \theta} + j \sin \psi \right) \frac{D}{F}, \quad (25b)$$

$$i \cdot \frac{\mathbf{k}}{|\mathbf{k}|} = \cos \Omega = \frac{\cos \psi}{\sqrt{\cos^2 \psi + \sin^2 \psi \sin^2 \theta}}, \quad (25c)$$

and

$$\Omega = \cos^{-1} [1 + \tan^2 \psi \sin^2 \theta]^{1/2} \quad (26)$$

Examination of Eq. (26) shows that obliquity narrows the directional characteristics for almost all ψ .

OCEAN SPECTRUM

It is necessary to establish a relationship between the photographic spectrum thus far obtained and the real ocean spectrum. The connection is provided by

$$\mathfrak{F} \{ f(\mathbf{a} \cdot \mathbf{x}) \} = \frac{1}{|\mathbf{a}|} F\left(\frac{\mathbf{s}}{a}\right), \quad (13c)$$

where

$$\mathfrak{F} \{ f(\mathbf{x}) \} = F(\mathbf{s}). \quad (27)$$

Extending this to two dimensions and operating on the Fourier transform

$$\mathfrak{F} \{ \phi(X, Y) \} = \bar{\phi}(K_X, K_Y) \quad (28)$$

yields

$$\mathfrak{F} \left\{ \phi \left(\frac{X}{\beta_x}, \frac{Y}{\beta_y} \right) \right\} = \beta_x \beta_y \bar{\phi}(\beta_x k_x, \beta_y k_y). \quad (29)$$

Equations (28) and (29) represent the same quantity, the β coefficients being in effect only a change in the dimensions used to measure X and Y. Therefore,

$$\bar{\phi}_{\text{ocean}}(K_X, K_Y) = \beta_x \beta_y \bar{\phi}_{\text{photo}}(\beta_x k_x, \beta_y k_y) \quad (30)$$

where the word subscripts are used to keep track of the "space" in which the quantity is defined. Invoking Eq. (19) once again yields

$$\Phi_o(K_X, K_Y) = \int_{K_X}^{K_X + \Delta K_X} |\bar{\phi}_o(K_X, K_Y)|^2 dK_X dK_Y \quad (31)$$

and

$$\Phi_{\text{ocean}}(K_X, K_Y) = \beta_x \beta_y \Phi_{\text{photo}}(k_x, k_y). \quad (32)$$

In this case the β 's are the factors relating the scales on the sea and photo and are given by

$$\{\beta_x, \beta_y\} = \frac{H}{F \sin \theta} \left\{ \frac{1}{\sin \theta}, 1 \right\}; \quad (33)$$

hence one obtains

$$\Phi_{\text{ocean}}(K_X, K_Y) = \frac{H^2}{F^2} \csc^3 \theta \Phi_{\text{photo}}\left(\frac{H}{F} \csc^2 \theta K_X, \frac{H}{F} \csc \theta K_Y\right). \quad (34)$$

LONG-WAVELENGTH SPECTRUM

Optical analysis performs exactly and very rapidly a mathematical transformation which is otherwise lengthy and somewhat difficult. The limitations of SPA basically reside in the difficulty encountered in recording an appropriate photograph. The long-wavelength range of the water-wave spectra requires a photo taken from an altitude sufficiently high such that the transform falls outside the dc term. From such altitudes, many difficulties may arise which would preclude good photography, i.e., haze and cloud coverage. Wave photos of wide angular coverage from lower altitudes would have too much perspective distortion to yield reliable optical spectra. It is possible, however, to extract such low-frequency information from a single photograph by analyzing the intensity variations along a line through the reconstructed image and by removing effects of differing perspective. Then if a number of such photos are analyzed and the spectra are averaged, the long-wavelength spectral components can be measured with good statistical accuracy.

The method used is to scan the photograph with either a microdensitometer or a flying-spot scanner, to digitize the results, and to perform the spectral calculations by computer. A new scan direction is required for each wave direction. Either the proper scan direction can be obtained from the directivity of the optical spectra, or the synoptic situation can be used to infer the proper direction.

It is possible to approximate optically the technique of averaging spectra. The approach makes a square matrix or mosaic of individual photos and rephotographs the composite to obtain a single photo of appropriate size. The resulting spectrum contains lower frequency information. This technique creates about as many problems as it solves and to date has proved decidedly inferior to the scanning technique.

Part of the great utility of the optical technique resides in its ability to handle simultaneously many data points in many combinations. It should not be too surprising that when the number of data points and necessary combinations is significantly reduced, scanning and digital-computing techniques can again be competitive.

SLOPE, WAVEHEIGHT, AND FREQUENCY SPECTRA

The techniques for obtaining a real ocean spectrum have been outlined. Normal-angle spectra are, however, rather more unfamiliar to most scientists than energy spectra of waveheights. Making the transformation to more familiar territory (first to slope spectra, then to waveheight spectra, and finally to frequency spectra) involves assumptions which degrade the confidence in the final results. The first step is simple in that for water waves the tangent of the wave normal is almost always nearly equal to the wave normal itself, in spite of the fact that even at moderate wind velocities steep slopes do occur. Carrying the transformation further to obtain waveheight spectra is subject to further difficulties which are manifest in second order. Ignoring such difficulties, the author has found (4) that

$$\Phi(\phi; K, \psi) = K^2 \Phi(h; K, \psi). \quad (35)$$

This notation, $(\phi; K, \psi)$, is used to denote angle spectra as a function of wave number k and azimuth angle ψ . It is now necessary to transform once again to obtain frequency spectra, a quantity which has been measured for many years in the ocean. This introduces still another source of error relating to the only approximate equality existing in the classic equation

$$\omega^2 = gK, \quad (36)$$

where ω is the angular frequency of the assumed sinusoid. Equation (26) is strictly valid only for a single wavelength propagating on an infinite water surface in which there are no currents. Again, however, the deviations are surprisingly small and probably do not influence the first-order spectra to be obtained optically. (Recent measurements in the ultragravity region do exhibit first-order spectral variations, probably due to surface currents caused by the orbital motion of swell waves.) Within these limitations (2)

$$\Phi(h; \omega) = \frac{2\omega^3}{g^2} \int_0^{2\pi} \Phi(h; K, \psi) d\psi, \quad (37)$$

the functional dependence denoting waveheight spectrum as a function of frequency. This equation then can relate the optical measurements to measurements obtained by use of wave poles and can be used to evaluate optical measurements.

The distinction in the basic data does make complete agreement between optical and other methods unlikely. Wavestaffs are used to observe waveheights at a single point over a significant time interval, whereas optical techniques use data taken over some restricted time interval and over a significant portion of two-dimensional space. Thus ramifications of the stationarity and spatial homogeneity influence the different measurement systems quite differently.

EMPIRICAL SPECTRA

There exist empirical frequency spectral forms obtained from many observations of "fully developed" seas (3). These are one-parameter distributions relating wind velocity to the spectrum which results when equilibrium is established. Just as temperature describes thermal equilibrium, wind velocity seems to be adequate for ocean spectra at least at long wavelengths. Transient states are, however, many parameter states and present a significantly more complex problem.

A modern spectral form is due to Pierson-Moskowitz (3) and has the form

$$\Phi(h; \omega) = \frac{\alpha g^2}{\omega^5} \exp \left\{ -\gamma \left(\frac{\omega_0}{\omega} \right)^4 \right\} \quad (38)$$

$\alpha = 8.10 \times 10^{-3}$, $\gamma = 0.74$, and $\omega_0 = g U_{19.5}^{-1}$, where $U_{19.5}$ is the wind velocity at 19.5 m above the mean sea level.

As a consequence of this spectral form, many of the oceanographic observables are specified in terms of the wind velocity. Among these are

$$H_{1/3} = 2.14 \times 10^{-2} U_{19.5}^2, \quad (39)$$

$$\omega_{\max} = 0.877 U_{19.5}^{-1}, \quad (40)$$

$$\tau_{\text{ave}} = 0.81 \frac{2\pi}{g} U_{19.5}, \quad (41)$$

and

$$H_{\text{rms}} = \frac{1}{\sqrt{2}} H_{1/3} \quad (42)$$

$H_{1/3}$ is the average waveheight of the 1/3 largest waves; ω_{\max} is the frequency associated with the peak in the spectrum; τ_{ave} is the average period of the predominant wave; H_{rms} is the rms waveheight.

Using Eqs. (37) and (38), it is possible to express the directional spectrum in the form

$$\Phi(h; K, \psi) = K^{-4} P(K, \psi), \quad (43)$$

in the region for which the exponential factor is constant, where $P(K, \psi)$ is a dimensionless "pattern" of the spectrum, for which the integral from 0 to 2π equals the constant α in this region. Thus optically the function usually plotted is

$$K^2 \Phi(\phi; K, \psi) = K^4 \Phi(h; K, \psi) = P(K, \psi). \quad (44)$$

This removes the strong trend in the spectrum as wavenumber varies. Further, it is easy to determine the onset of the exponential factor, enabling one to assign a wind velocity to a given spectrum, assuming equilibrium is established.

Substituting the spectral form of Eq. (43) into Eq. (37) and using the Pierson-Moskowitz spectrum on the left, one obtains

$$\frac{\alpha g^2}{\omega^5} \exp \left[-\gamma \left(\frac{g}{\omega U_{19.5}} \right)^4 \right] = \frac{2\omega^3}{g^2} K^{-4} P(K) \quad (45)$$

using, $\omega^2 = gK$ and $e^x = 1 - x$, $x \ll 1$, yields

$$\alpha \left[1 - \gamma \frac{g^4}{\omega^4 U_{19.5}^4} \right] = 2 P(K). \quad (46)$$

Using full optical analysis, the right side can be calculated to give the value of k for which some fraction of saturation is reached, and the left side brackets must be the same fraction. Thus $U_{19.5}$ is estimated.

TRANSIENT STATES: STATIONARITY AND HOMOGENEITY

The real wind over a region of deep ocean varies with time and space, whereas the major dissipation and propagation characteristics are largely invariant (ignoring boundaries, oil slicks, etc.). Thus observed spectra are often a superposition of spectra generated at different times and places. Usually a given area is designated as having "sea," i.e., a portion of the spectrum resulting from local winds, and "swell," i.e., spectra resulting from past storms at other locales. The wave dissipation per unit length can be thought of as being almost a constant; thus short wavelengths damp out more rapidly than longer wavelengths. A spectrum can exhibit a number of peaks, such as an ultra-gravity-wave peak due to inhomogeneous values of the wind velocity, a gravity-wave peak due to the stationary component of the local wind, a long-gravity-wave peak associated with some distant storm, and perhaps a very-long-wave peak due to tidal and other motions. There may even be a capillary-wave peak at light winds arising from the local winds but caused by the effects of the surface tension altering the spectral form for equilibrium. Such a transient state is very common, and no one parameter description can be adequate for a complete ocean definition.

Sea Photo Analysis provides a technique whereby some of these effects can be studied. Photographs can be taken at one place as a function of time or after short time intervals over separate parts of the ocean. In this way stationarity and homogeneity can be evaluated and the effects on other sensors estimated.

TOWER INSTALLATION

The experimental manifestation of the preceeding theoretical considerations at the Naval Undersea Research and Development Center (NURDC) tower in San Diego was as follows. A 35-mm-format Nikon camera with a 50-mm lens, a horizontal polarizing filter, and a 250-exposure back was detachably mounted to the tower at a point 62 ft above mean sea level. The camera mount was affixed to the wench driven sled to allow the camera to be raised or lowered as needed for film changes or demounting. The mount was designed to secure the camera in a 40° depression angle from the horizon with the 35-mm-film

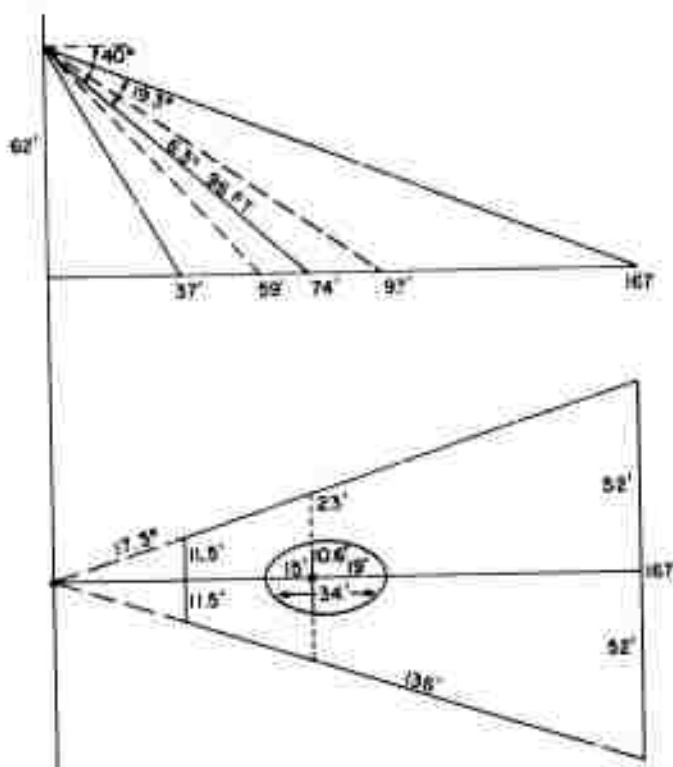


Fig. 5 — Projections of the camera field-of-view onto the ocean surface

dimension subtending depression angle and the 24-mm axis covering azimuth angle. The optic axis normally was oriented in a due west direction, although provisions were made to accommodate a due north look angle. Figure 5 shows the geometric configuration.

Previous tests had shown that the light variations were sufficiently large (as a function of time) to preclude the use of a high-contrast, low-latitude film. Consequently all the photographs were taken using Panatomic X film, which has an ASA rating of about 32 and a gamma of less than 1. Exposures normally ran 1/125 with an aperture of $f/2.8$. Photographs of the ocean surface were taken every 15 s. This allowed the 250-exposure capacity to provide a data run matching the normal 64-min radar run.

Although it was not mandatory to obtain absolutely calibrated spectra, fish-eye photographs were taken at various intervals during each day. This imagery was intended to allow absolute calibration of the spectral data should that be desired in the future. These photographs were taken by pointing the hand-held camera toward the horizon in the direction the 50 mm camera was aimed. The 180° or hemispherical field of view allows the relative luminance of the sky and the water to be determined directly, improving the accuracy of the Eqs. (7) and (8) used in calculating wave sensitivity. This also allows a direct measurement of the subresolution rms slope.

DATA ANALYSIS

The optical data analysis uses a lens with an equivalent focal length of 92 cm for normal bench length. The Gaussian beam had an equivalent uniform illuminated aperture 11 mm in diameter. This translates to an area on the sea as indicated in Fig. 5. This spot size is commensurate with the range-resolution cell chosen in the radar design. Part of the data was processed with an effective focal length of 46 cm. The spot size in this case is 5.5 mm in diameter.

The normal means of reading out the relative spectral amplitudes, (Eq. (23)) is to scan a photomultiplier through the transform light distribution. This, however, proved to be far too slow to conveniently analyze the large number of photographs accumulated during the field work. This is true even when only those data runs with a significant overlap with the other sensors are considered. To facilitate the data reduction, two masks were fabricated which could be moved through the light distribution and sequentially read the integrated light intensity at some mean wavenumber and wavenumber interval. This allowed a tabulation of the light intensities falling in a fixed-percentage bandwidth at a set of discrete ocean wavelengths. Figure 6 shows the design of one of the masks. This mask is backed by a slit of proper size to allow only two holes to transmit light at any time; one hole is for half the spectrum, and the other hole is for the ambiguous other half. It can be seen that the aperture increases in diameter in direct proportion to the wave number. This tends to yield both a measured constant light power and a constant fractional wavenumber interval, i.e., the measured intensities are directly proportional to $P(K, \psi)$ of Eq. (44).

The use of the masks was not without difficulty. The mask must be positioned quite accurately, especially for the very low wavenumbers. Physical tolerances, however, provide a limit to these accuracies, with the consequence that the small pinholes very near the dc term show extreme fluctuations in measured light intensity. As a result, the validity of the longest wavelengths analyzed is suspect, although the inaccuracies become insignificant for the range of wavelengths comparable with the Bragg wavelengths for the radar frequencies used in the radar system.

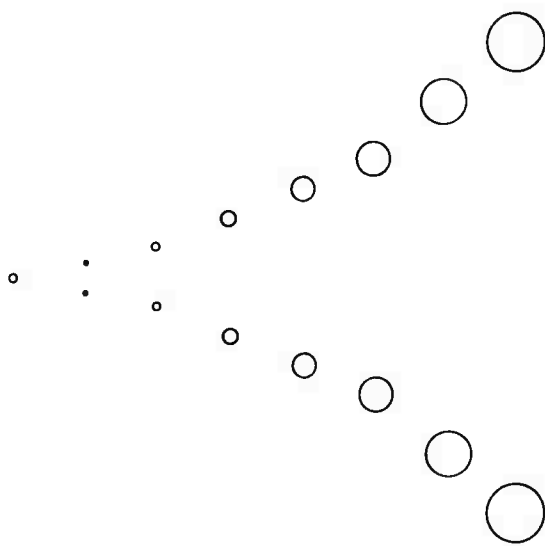


Fig. 6 — Mask design (enlarged 5 times)

EXPERIMENTAL RESULTS

Figures 7 through 70 represent the basic results of the optical data analysis. Presented are eleven distinct runs on eight different days. Data were taken on other days, but the analysis was sufficiently lengthy to preclude total analysis and made it possible to reduce only those data having a significant overlap with other sensors. In the succeeding paragraphs, each data run is discussed to point out the significant features of the data and to indicate the limitations pertaining to the interpretation of the results. Most of the graphs are plotted with the negative sign of the ordinate suppressed. Increasing spectral energy is therefore in the positive y direction. The abscissa is plotted as Greenwich Mean Time (GMT), which differed by 7 hr from the local time. For all graphs the spectra was sampled at 15 s intervals.

Figures 7 through 10 are plots of the spectral variation for the Sept. 16 run between the times of 1637 and 1735 GMT. The mask used averaged the spectrum over a $\pm 25\%$ band of wavelengths. This average operates over both dimensions in wavenumber space. It is evident from these curves that there are large deviations from the mean of the spectral amplitude over this time period with fine structured variations superimposed. This is characteristic of all the runs. The large deviations, having an internal-wave-like periodicity (IW-like), can arise due to nonstationary wind conditions, inhomogeneous wind field, or internal-wave (IW) effects. The fine structure could be due to at least four causes, which are listed in the order of importance. First, the folding of the spectra by the existence of swell. This effect is most predominant and holds for all the measurements made during the experimentation at the tower. Second, it is possible that the ocean surface is composed of numerous wave packets or patches of fairly monochromatic energy. If the number of these packets in a given analyzed area is small, the expected variation could be quite large. Third, there is some positioning error involved in the mask placement from frame to frame. As a result there is an imprecision of the data which is most significant for the long wavelengths but becomes minimal as the wavelength is shortened. Finally, there is a small variability associated with the mean exposure level of the photographs. This factor is quite small and was measured during the data analysis and found to be insignificant. As with all the results of this experiment, the magnitude of the IW-like variability diminishes toward the shorter wavelengths. This is most likely due to the "frequency" response, referred to in optics as the modulation transfer function (MTF), of the camera-film system. The wave information is of sufficiently low contrast that the "roll off" is significant as the recorded film wavenumber approaches 20 lines/mm.

Figures 11 through 14 also pertain to Sept. 16, but in this case the camera was looking north. This orientation, because of wave-visibility considerations, predominately measures spectral components perpendicular to the internal waves. Such information is of value in analyzing the coupling at high angular differences between the wave systems. Again there is evidence of the fine structure associated primarily with the effects of under-sampled swell. There is, however, the longer term fluctuations probably due to internal waves or due to variations of wind velocity or direction. A decision between the causes would require a cross-correlation with the other sensors aboard the tower, such as the thermocline fluctuation and wind records. Compared with the data taken during the morning, the long-term variations are significantly smaller, about 3 dB compared to 7 or 8 dB, a result probably due more to the look angle than to the time difference.

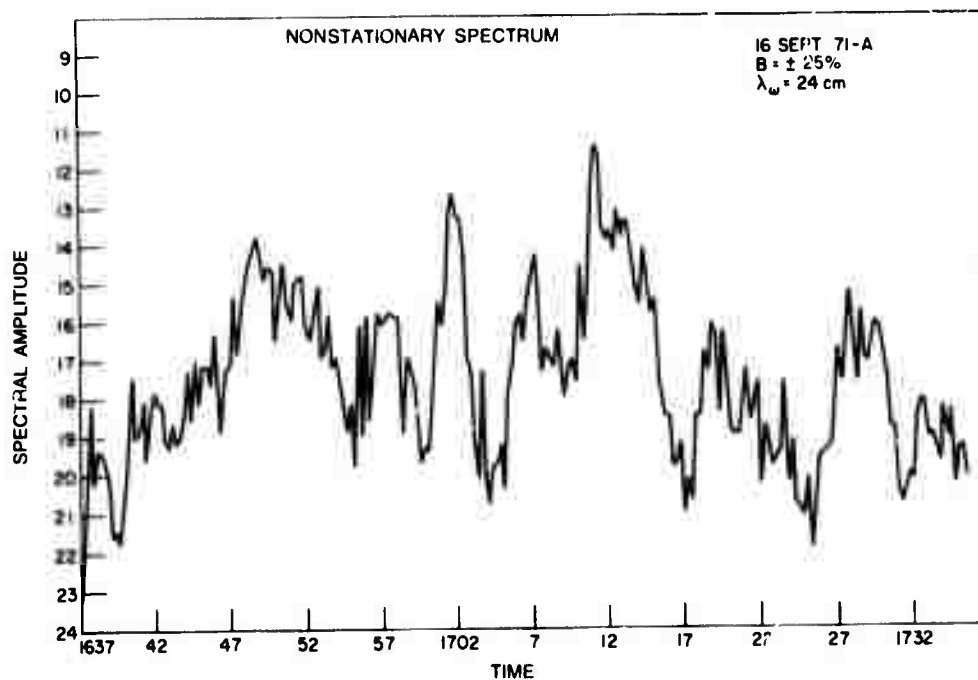


Figure 7

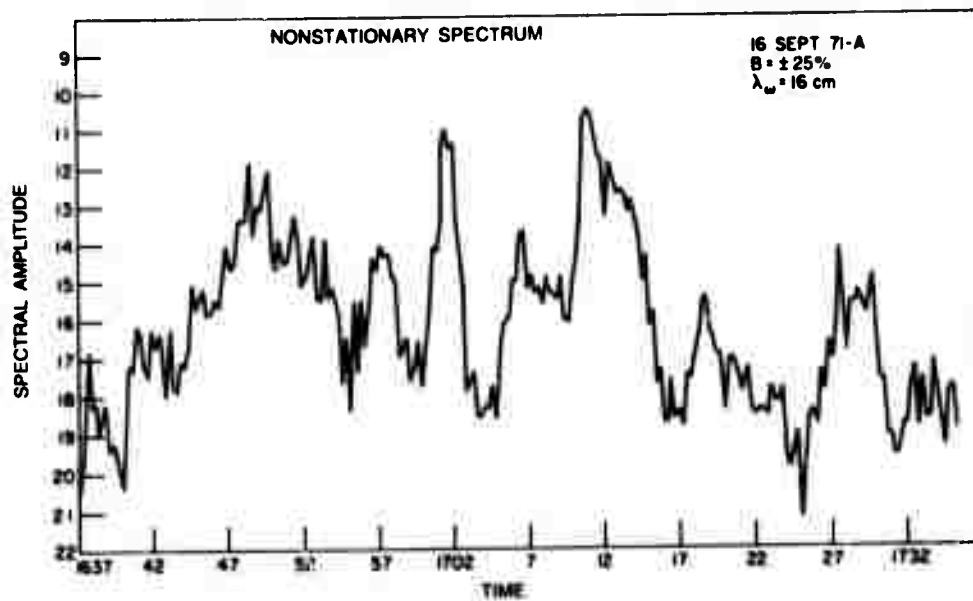


Figure 8

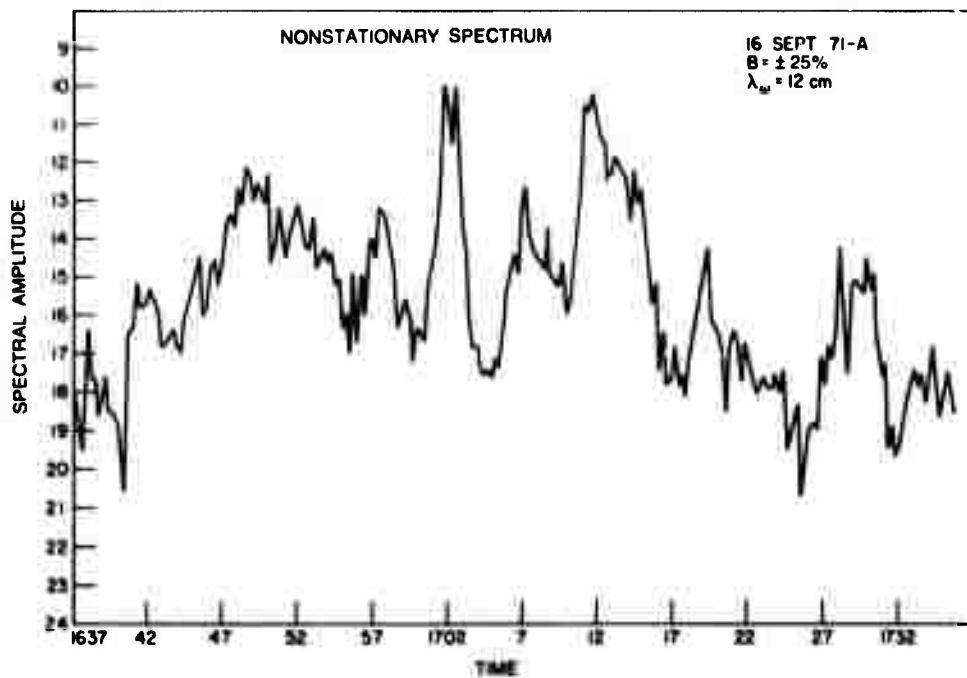


Figure 9

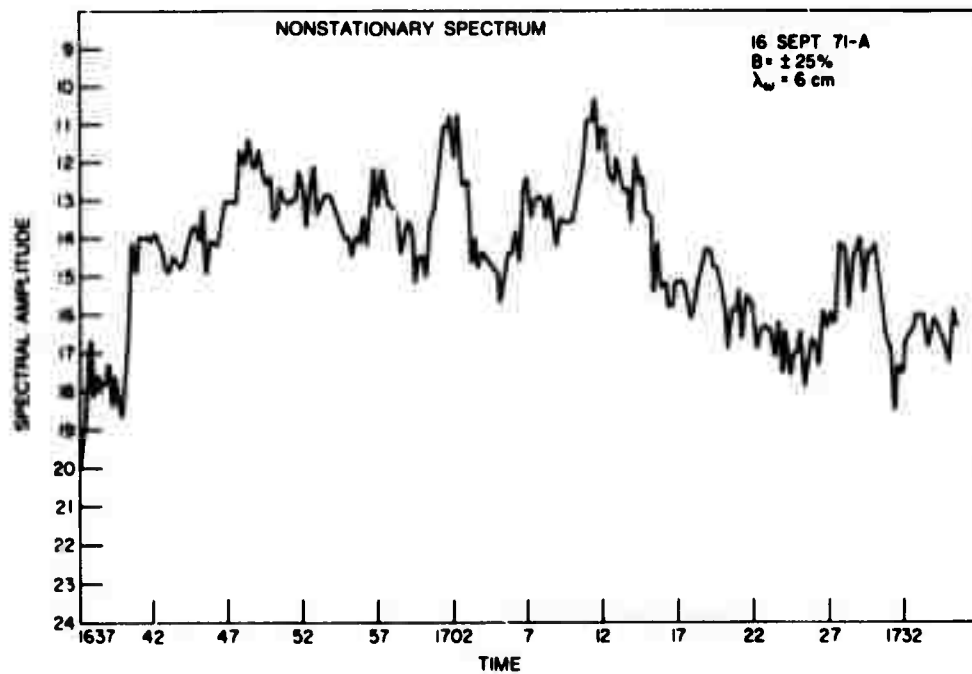


Figure 10

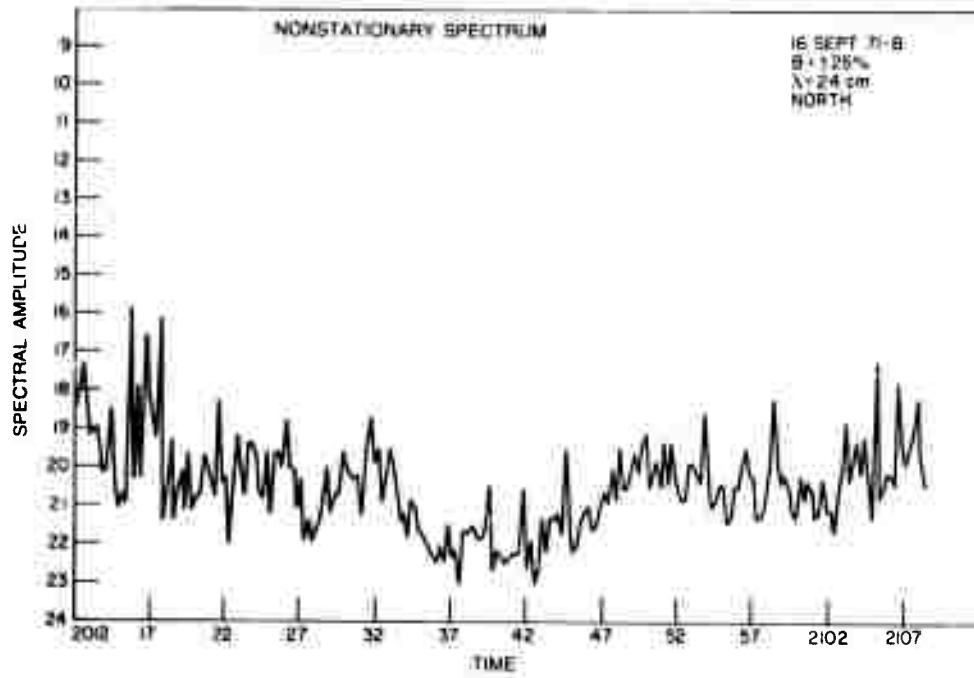


Figure 11

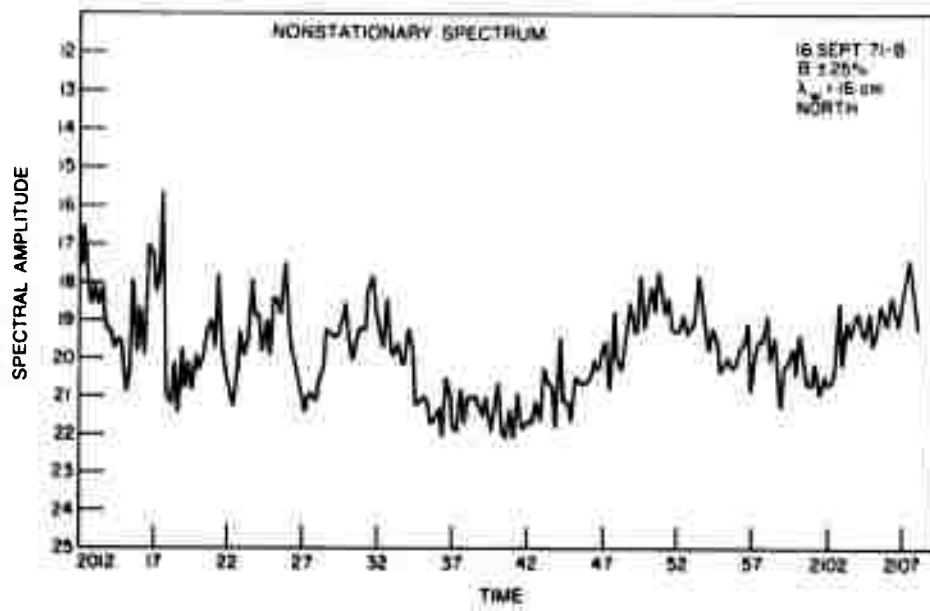


Figure 12

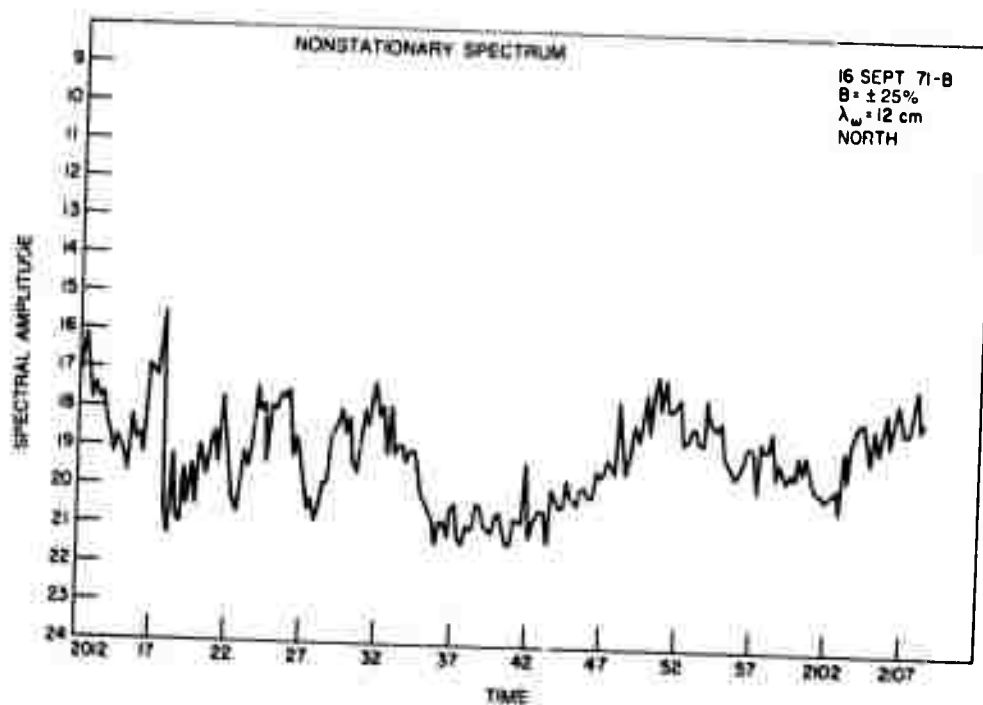


Figure 13

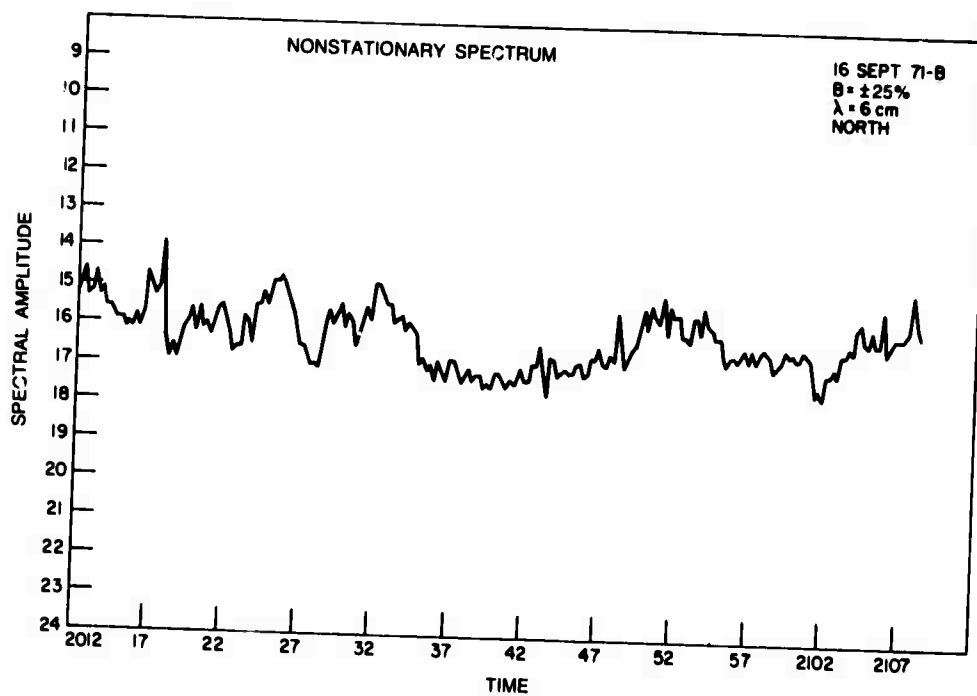


Figure 14

Figures 15 through 18 are the results of optically analyzing the photographs taken on Sept. 28 from 1846 to 1943 GMT. Here there are two regions of very strong suppression of the wave spectrum. At about 1852 and 1900 GMT, the spectral amplitude decreases by a factor of ten. In all probability, such extreme variation is the result of a "slick"-like section of the water. The width of the slick is about 3 to 4 min in time, probably corresponding to 18 to 24 m of spatial extent if the slick is moving at a rate of 10 cm/s. Visible slicks were not normally this wide. It is possible that the current-wave interactions which tend to compact biological material may have a longer range effect than that apparent to the eye. Again, correlation of these figures with the slick photography might prove to be of value. The 24-cm curve shows considerable variability of the fine structure. This might result from inordinate positioning errors in the data reduction, but this is unlikely, since the same variability extends into the higher frequencies as well. A more probable reason is that a fairly significant swell existed on this day which caused severe changes in the spectrum, due to strong orbital currents. The fact that the variability remains when the analyzed region is many wavelengths long in both dimensions supports the swell hypothesis.

Figures 19 through 21 display the variation in the spectrum for Oct. 1 from 1628 to about 1731 GMT. For this run the mask used averaged over only a $\pm 5\%$ region in wavenumber space. With this more restricted frequency-plane average, the fine structure variability is increased significantly. There is a strong trend in the data with evidence for IW period modulation of small magnitude. The 6-cm curve shows the small amplitude modulation clearly, but with such a strong trend, probably due to a changing wind, this fluctuation may also be due to the temporal instability of the wind field.

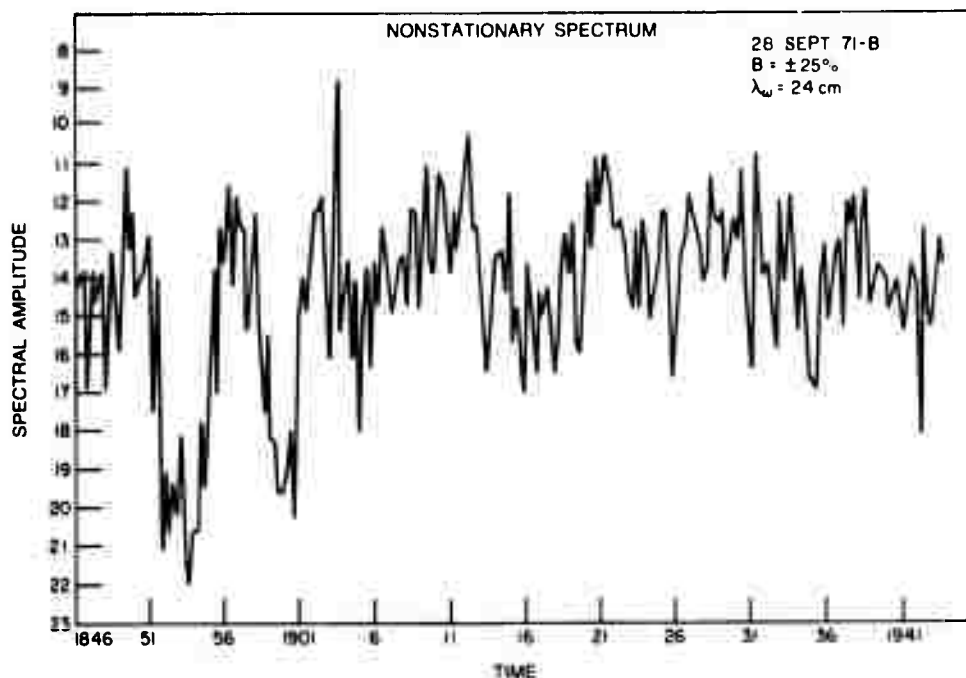


Figure 15

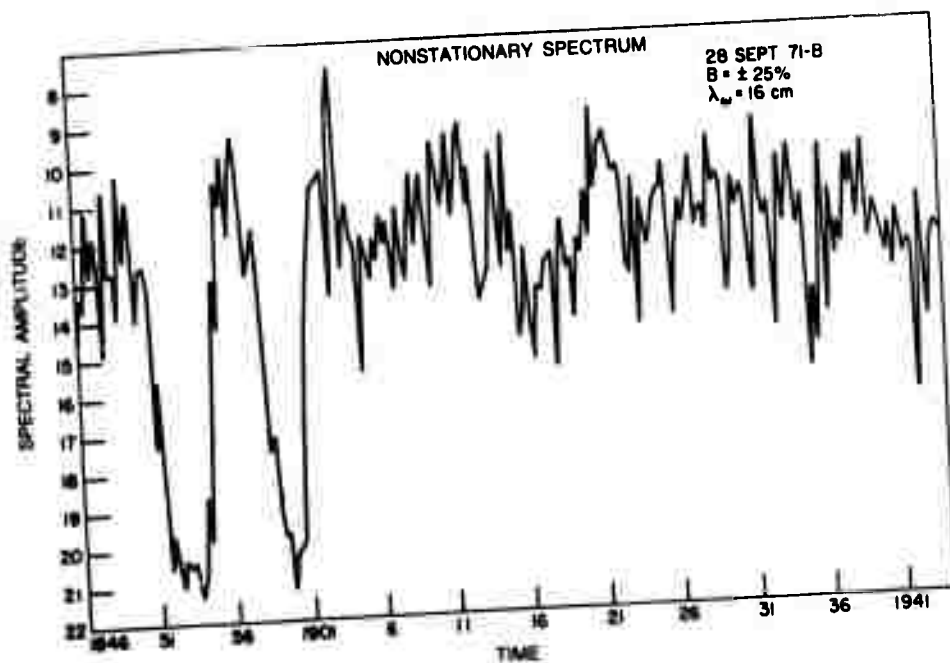


Figure 16

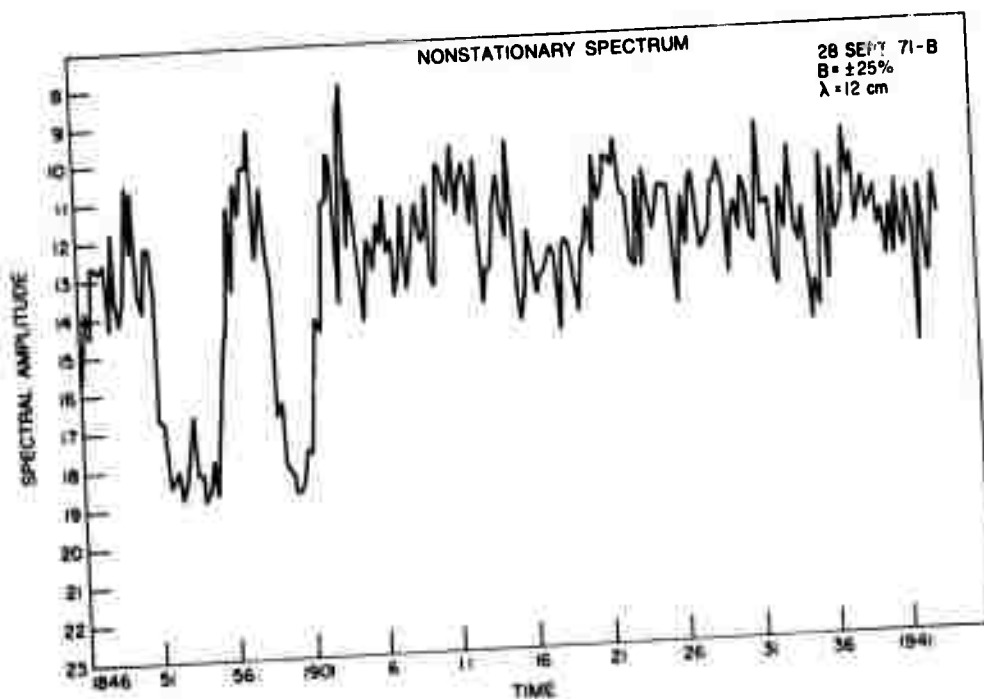


Figure 17

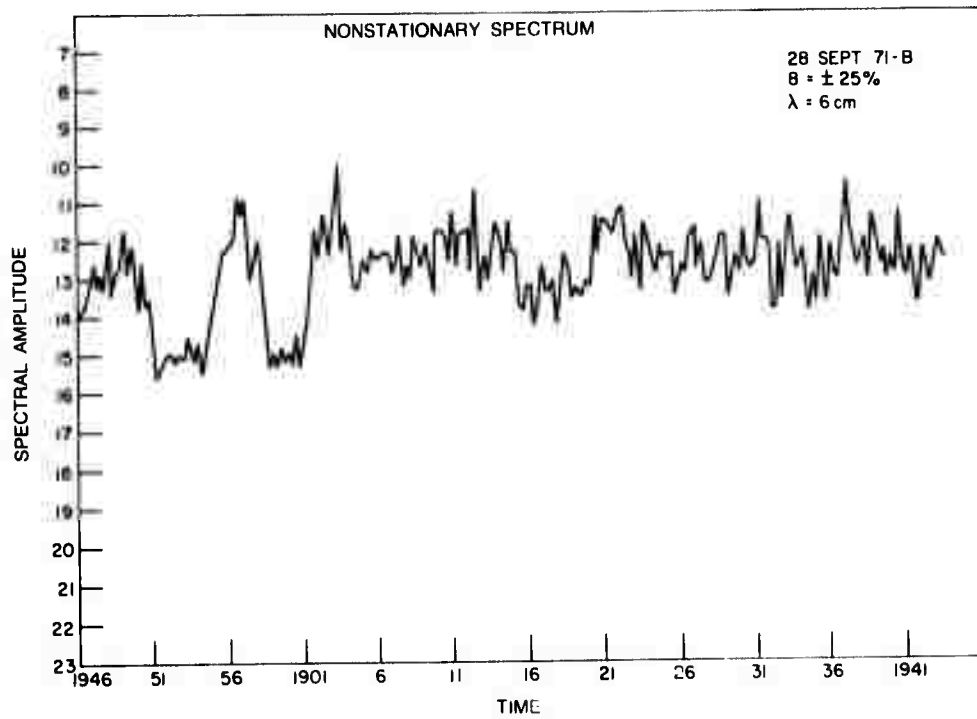


Figure 18

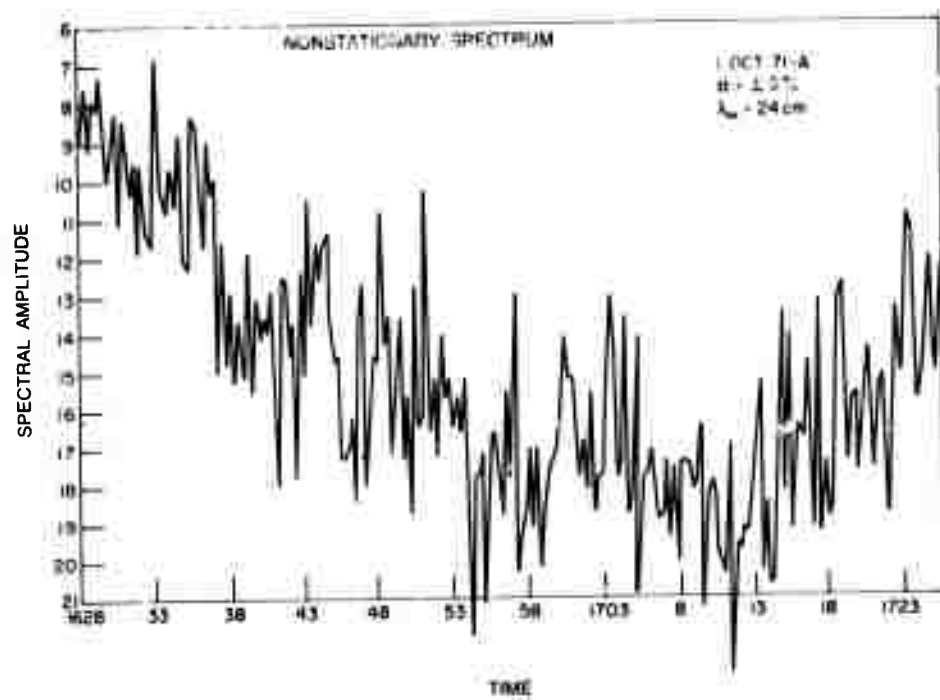


Figure 19

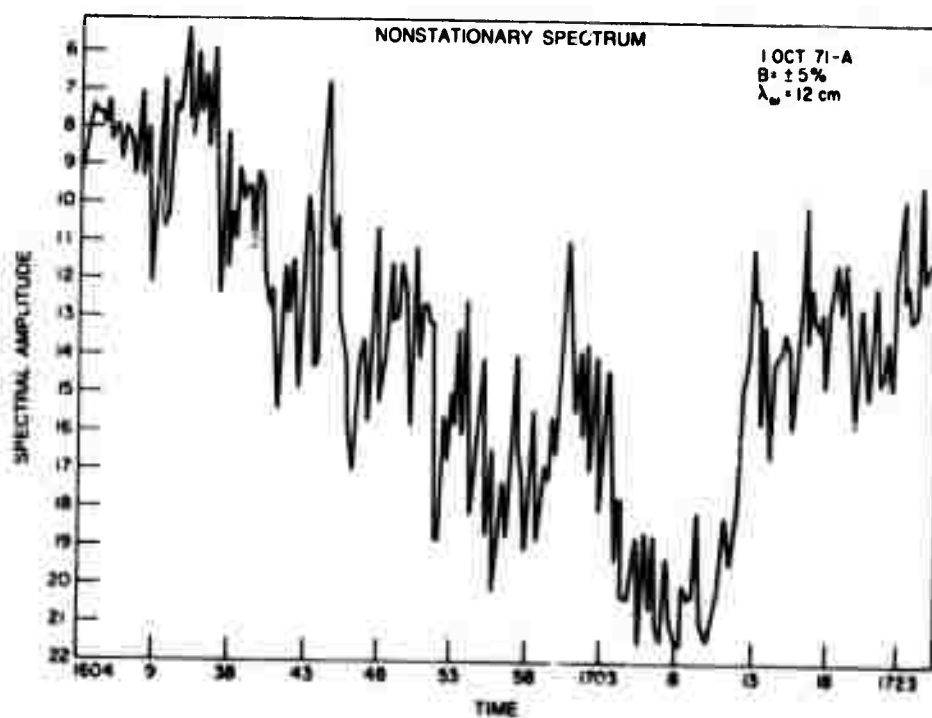


Figure 20

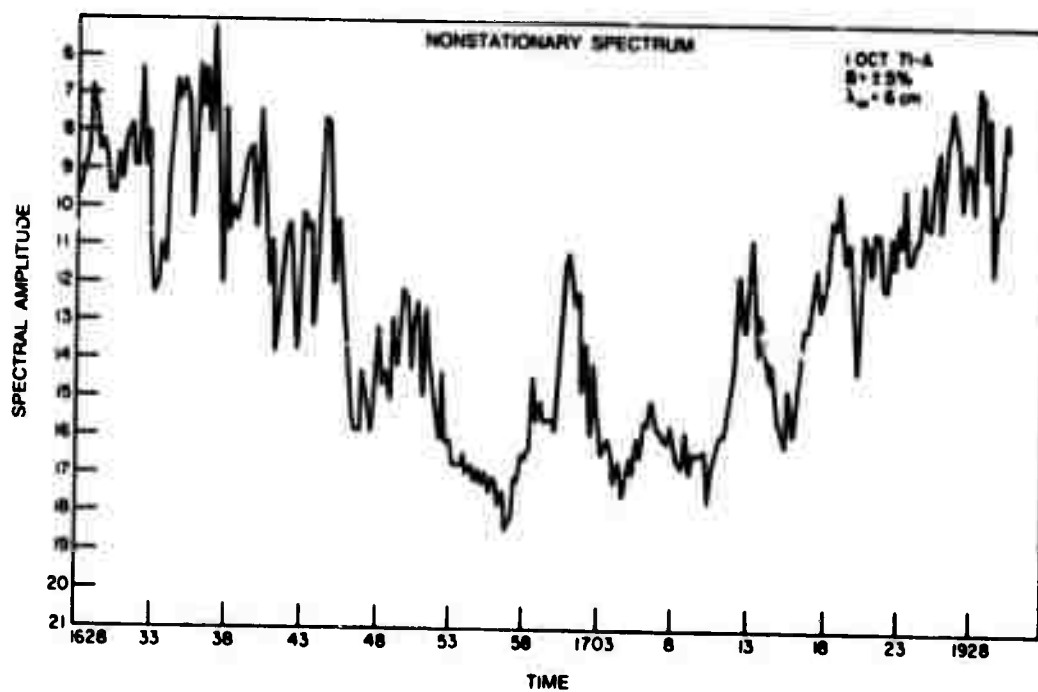


Figure 21

Figures 22 through 29 are time histories of spectral fluctuations for Oct. 4 from 1835 to 1928 with a $\pm 5\%$ frequency-plane average. This is one of the most unique sets of data accumulated during the entire program. During this time interval, the wind record shows the wind to be quite constant in direction and magnitude. During the entire run, the wind was $270^\circ \pm 30^\circ$, and the magnitude was between 4 and 6 knots, except for the interval 1902-1905, during which it rose to about 7 knots. The time histories, therefore, are very closely those for an equilibrium condition. The graphs show that there are two slick-like regions, one occurring at about 1849 and another at about 1923. The suppression of the ultragravity waves at these times is about 10 dB. During the period between 1855 and 1905, the wave spectra rose about 3 dB above the equilibrium level, just before the wind exceeded the 6-knot bound at 1902. This region of the internal waveform is most likely a region of differential roughening due to the interaction of the internal-wave/surface-wave system. A further anomalous feature is the very steep "recovery" after the first slick at 1850. Just to the rear of the slick, the spectral amplitude is seen to rise for a very restricted time interval and then fall back about 3 dB before the overshoot starting at 1856. The 35-min period for the arrival of internal waves is somewhat unusual but may be accounted for by the effect of tidal currents slowing the apparent rate of progression of the wave.

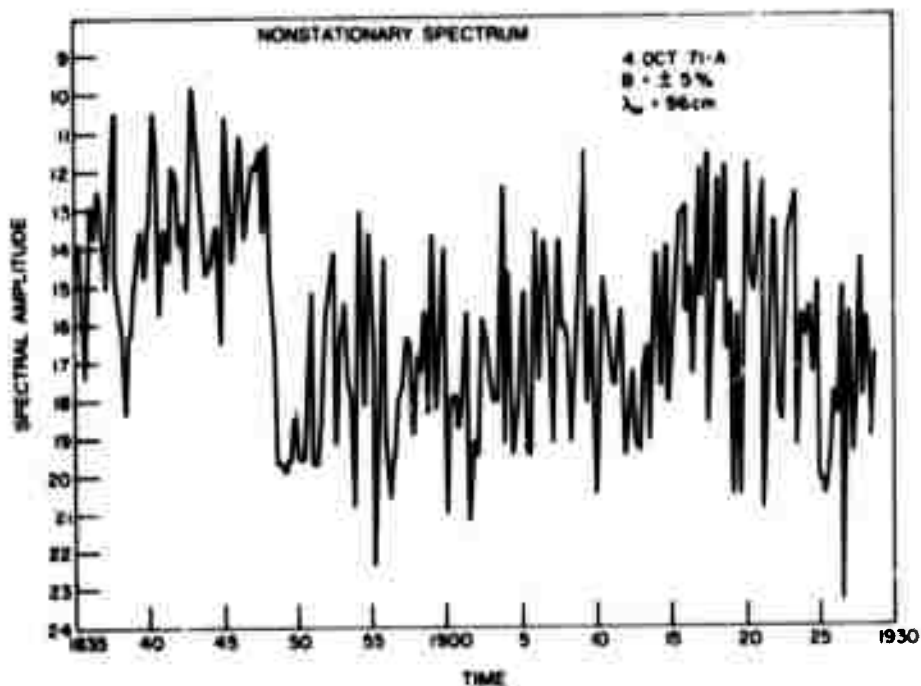


Figure 22

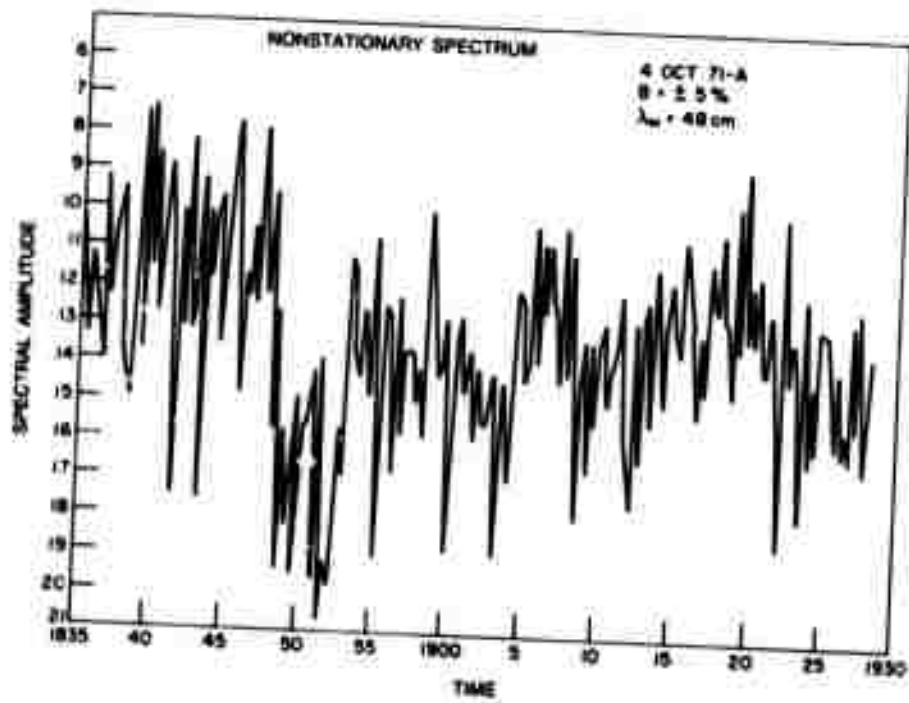


Figure 23

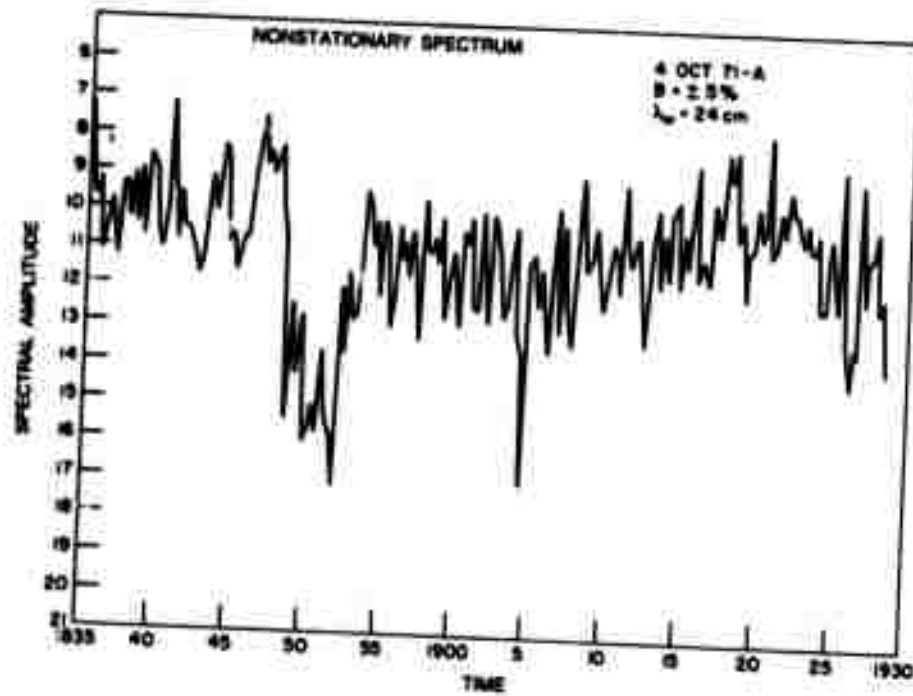


Figure 24

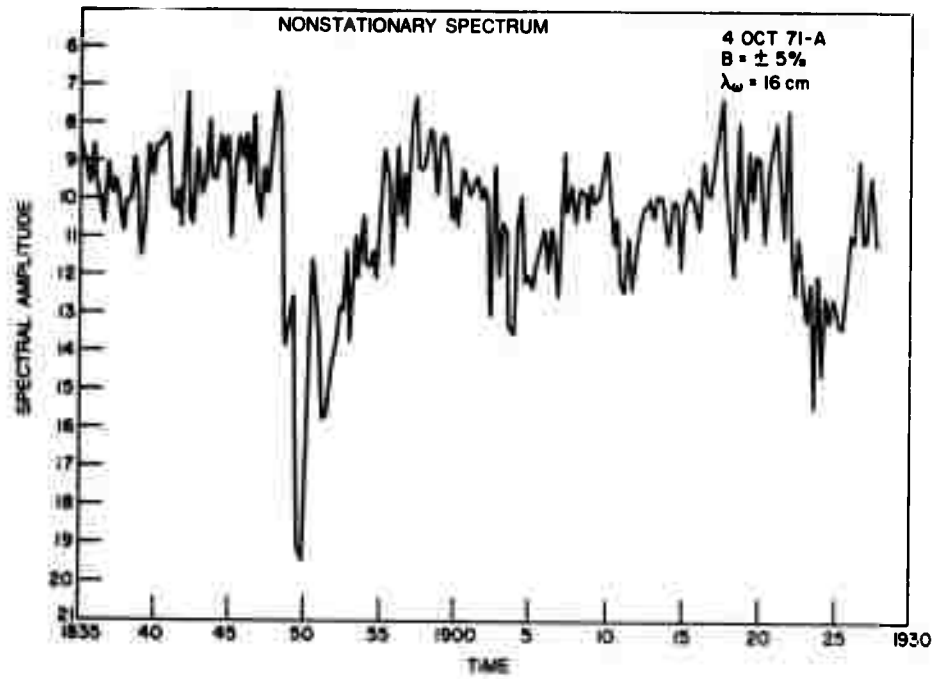


Figure 25

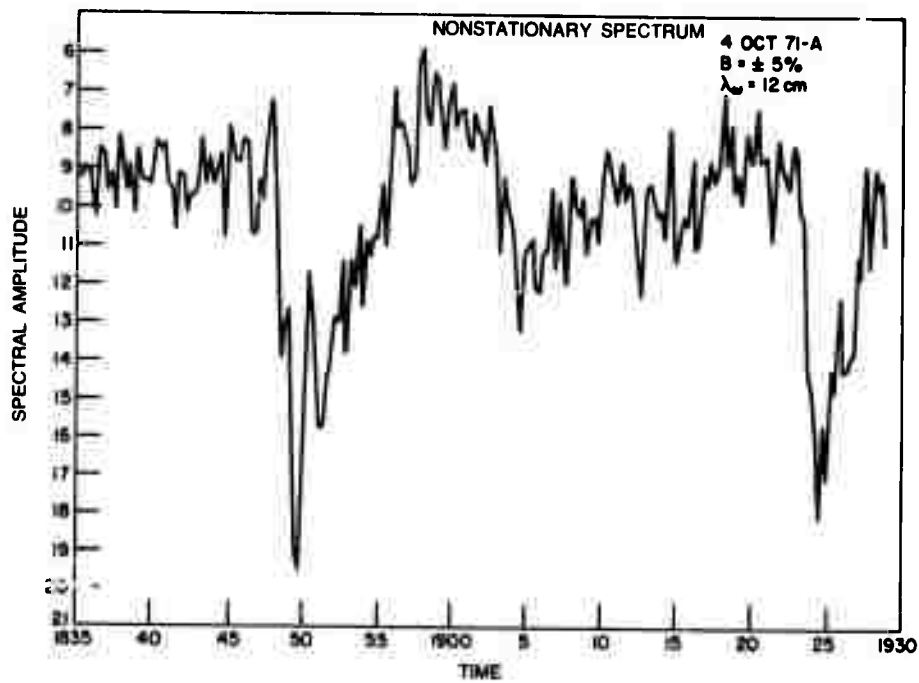


Figure 26

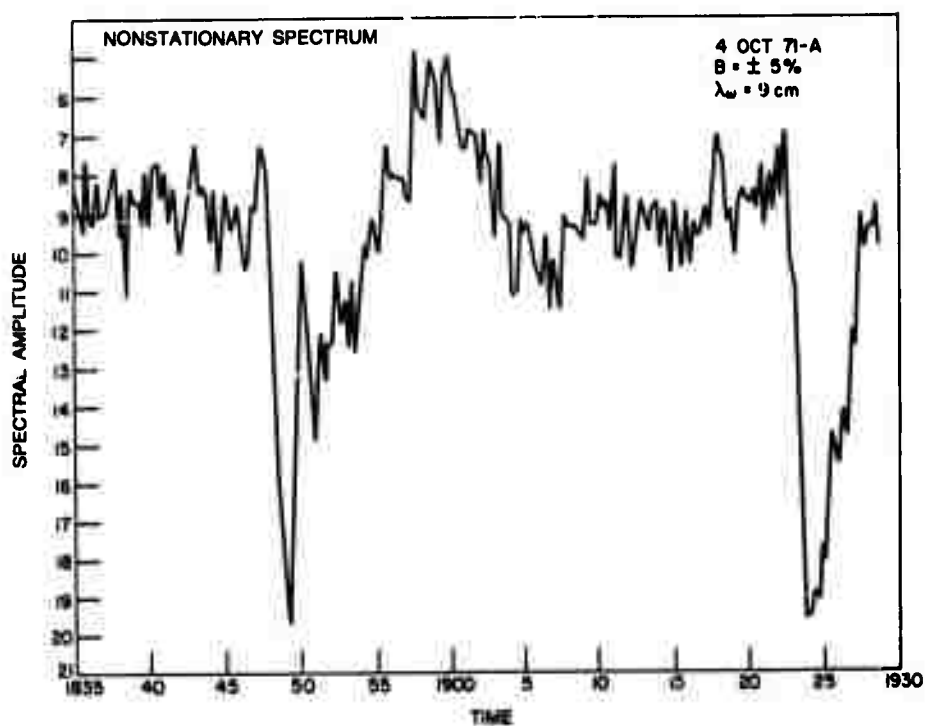


Figure 27

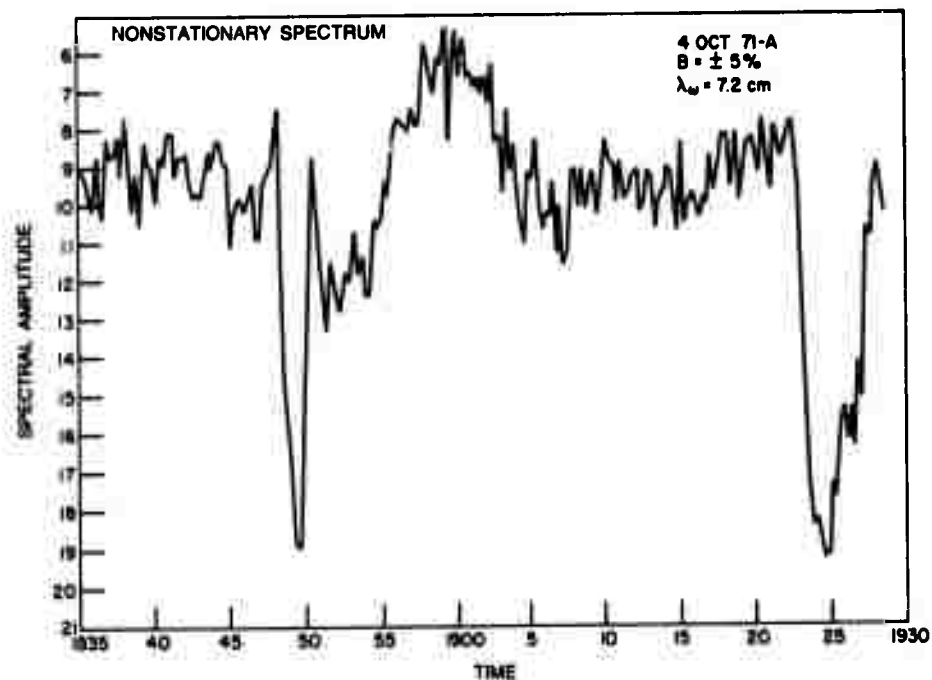


Figure 28

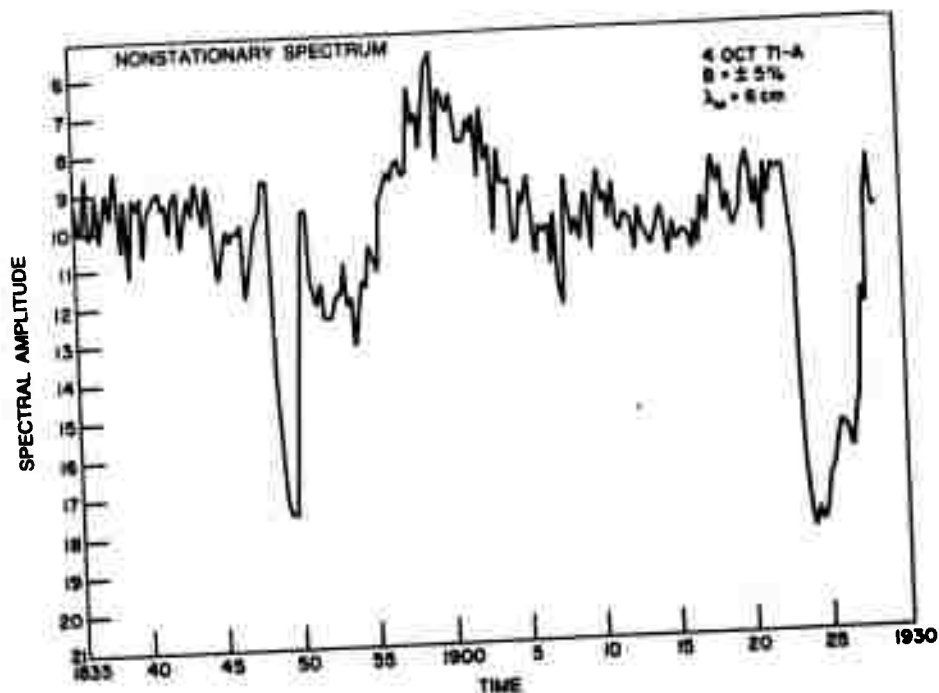


Figure 29

Figures 30 and 31 are a more detailed analysis of the interval about the slick occurring at 1849. These data were reduced quite differently from all the other data. First, to obtain some smoothing, the spectra were recorded on film by superimposing the exposure of four consecutive frames. This should reduce the effects of swell or any variability introduced by a small number of packets within one field of view. Second, a comparison was made for two spot sizes, 11 mm and 5.5 mm. Finally, the microdensitometer tracings used to relate the spectral amplitudes were smoothed by eye when taking the data from the density recordings. By these methods, a very considerable amount of temporal, spatial, and frequency-plane smoothing was achieved. Figure 30 used the 5.5-mm spot size. This spot was selected to provide higher frequency information, and the wavelengths plotted range from 2.9 cm to 26 cm. The anomalous rise just after the slick is quite evident at the higher frequencies but is seen to almost disappear at the 13-cm plot. Likewise, the overshoot occurring at 1900 is seen to abate at about the same wavelength. Figure 31 substantiates the conclusions. The strength of the dips are weaker than in Fig. 30. The reason must be the difference in spot sizes. For an effect smaller than the spot sizes, the smaller the spot size, the greater the ratio of maximum to minimum effects. In both of the figures there is evidence of the MTF of the camera-film system limiting the dynamic range available at the shorter wavelengths, i.e., the depth of the nulls are diminished as the analysis frequency increases. That this may be due in part to the bandwidth of the interaction process cannot be uniquely decided from this set of data alone.

Figure 30

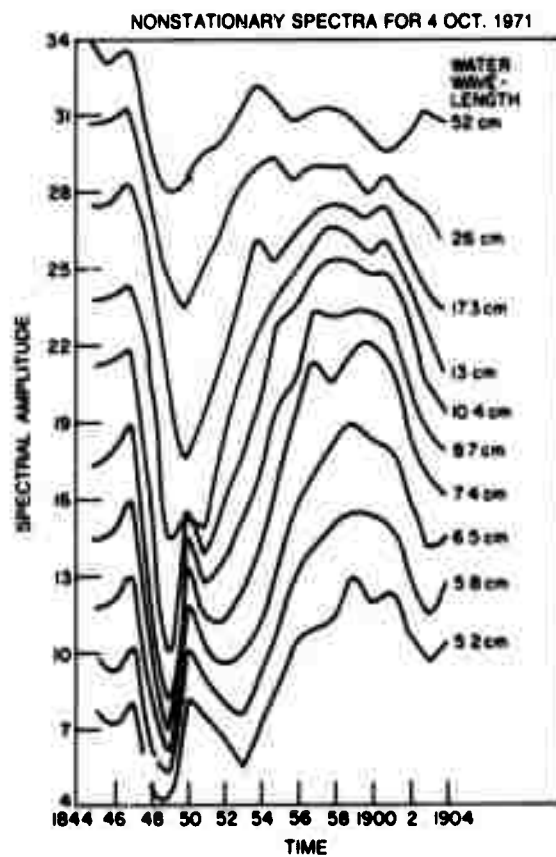
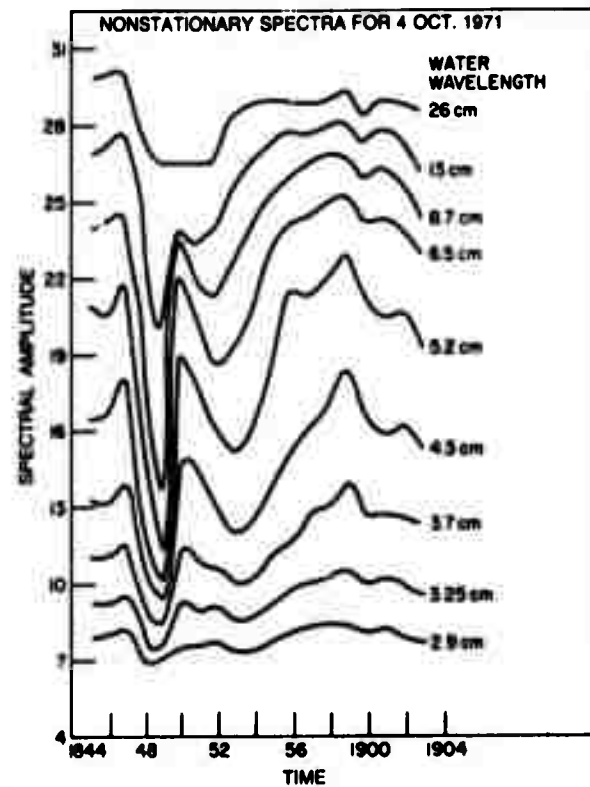


Figure 31

Figure 32 is a plot of the mean directionality in the wavelength interval from about 10 cm to 30 cm. For discussion purposes, the diffraction pattern of a scene can be visualized as a figure-eight pattern in wavenumber space. All the data to this point have been read along the major axis of this pattern. During the reduction, it was noted that there was a shift in the orientation of the figure-eight pattern with time (frame to frame). To measure this effect, an aperture corresponding to the wavelength interval of 10 to 30 cm was positioned in the frequency plane, and each scene was rotated to maximize the power spectrum caused some problem, because there seemed cases in which the spectrum was bimodal in the angular distribution. From the plot it can be seen that there is an important shift of about 7° occurring at the time of the slick. Such an effect is understandable if there is a difference in the propagation directions of the IW system and surface-wave system. In such a case the surface current due to the IW is a function of time (or space) and interacts strongly with those wavelengths whose phase speeds are comparable with the current speed. This should be most apparent at about 1.7 cm. Since the current will not interact with directional wave components perpendicular to it, only one component of the directional wavenumber will be affected. Thus a shift in the apparent direction of travel of the waves will be observed. The same considerations hold for the orbital motions of the swell. The fine structure in the directionality plot could be due to swell, and the gross features could be due to the internal waves. The basic accuracy of this measurement is not sufficient to rule out imprecision as the reason for the fine structure. The results can only be considered as indicative of what happened. More precise methods must be used to determine the centroid of the two-dimensional wave-number spectrum.

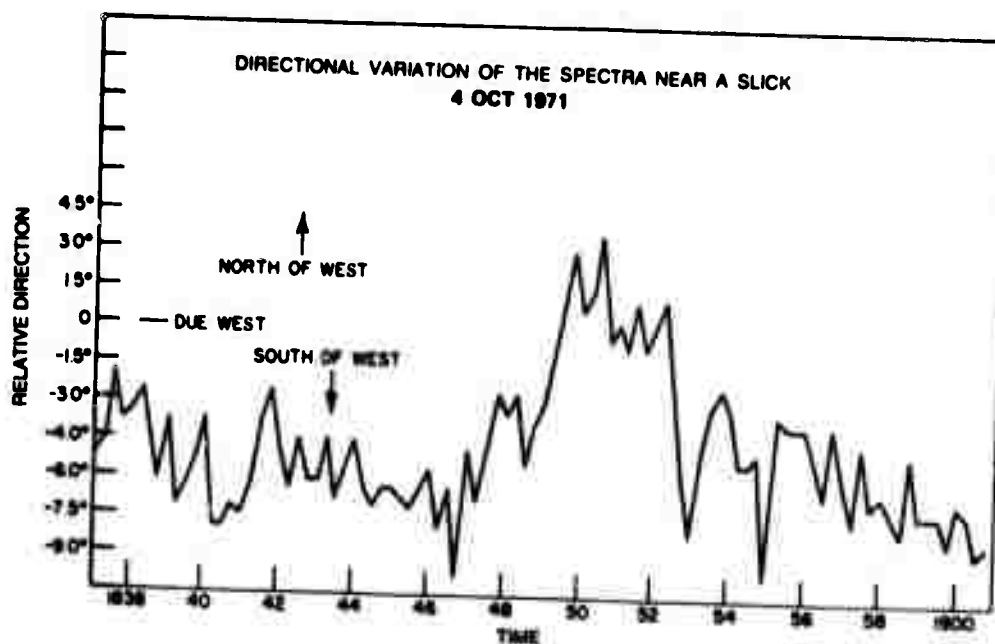


Figure 32

Figures 33 through 39 are the records for the period 1720 to 1816 GMT on Oct. 5. The ordinate on these plots is not labeled in dB but in a scale of volts, where 1V is equivalent to 3 dB of spectral power, again with suppressed negative sign. The averaging bandwidth for this and subsequent runs was $\pm 25\%$. This run is a good example of the effects of wind on the observed spectrum. During the interval, the wind was changing with a periodicity normally associated with internal waves. Consequently, the mixing of variable wind and internal waves precludes any identification of the individual mechanism. Figure 38 shows the tremendous variability involved in the 8-cm spectrum, which is almost directly correlated with the wind records. The two longest wavelengths evidence no such variability. The fine structure may indicate that spectral amplitudes in this domain are not greatly influenced by short-term wind fluctuations. The 96-cm curves do not seem to change significantly during the entire interval, due in part to measuring inaccuracies but further influenced by the potentially small number of wave packets per unit area generated by the light winds.

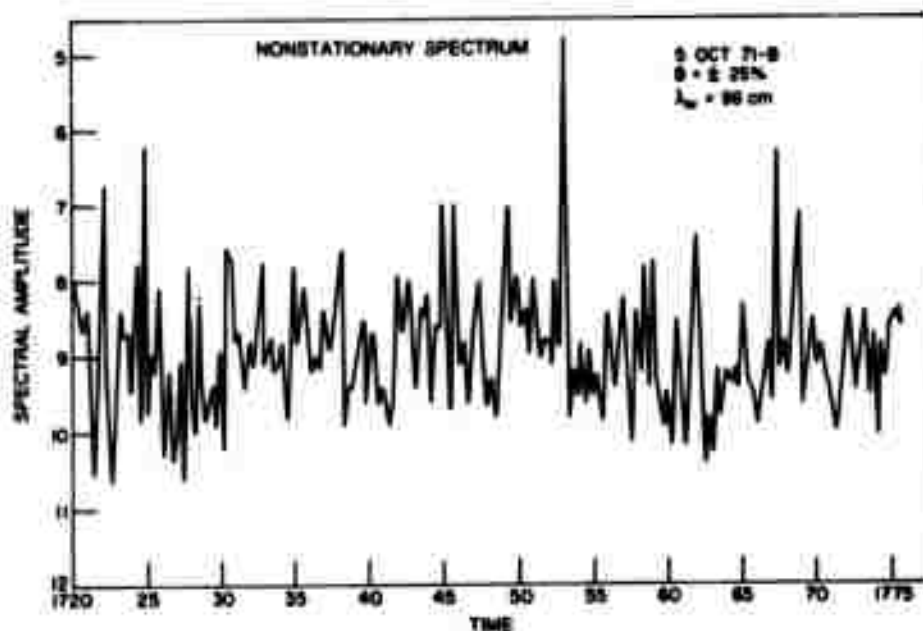


Figure 33

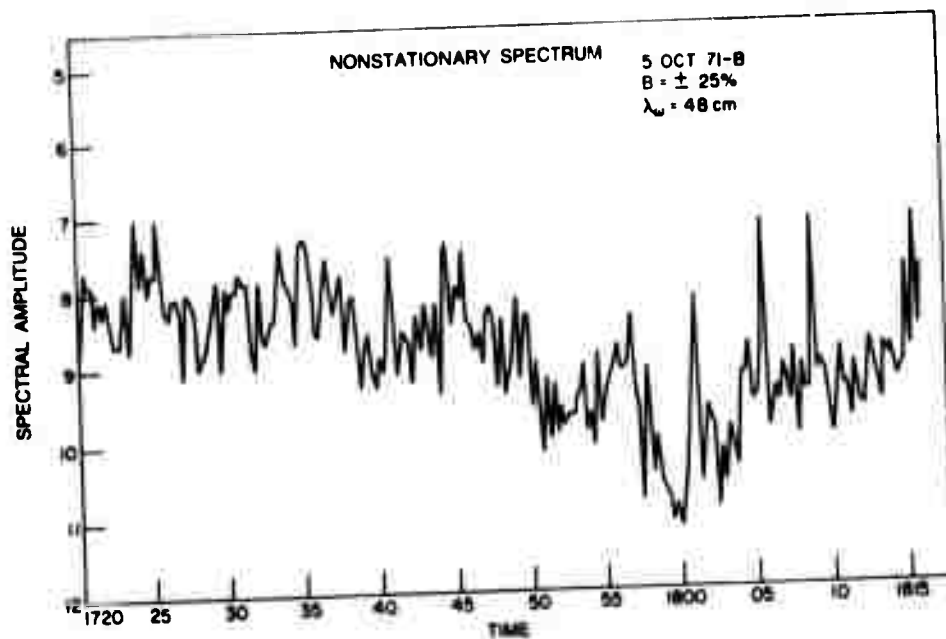


Figure 34

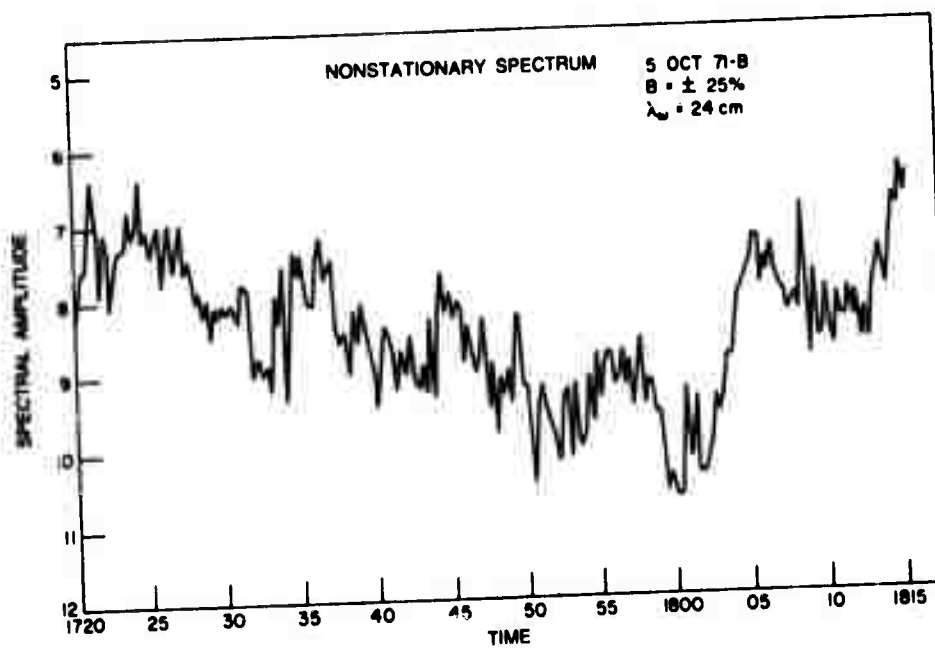


Figure 35

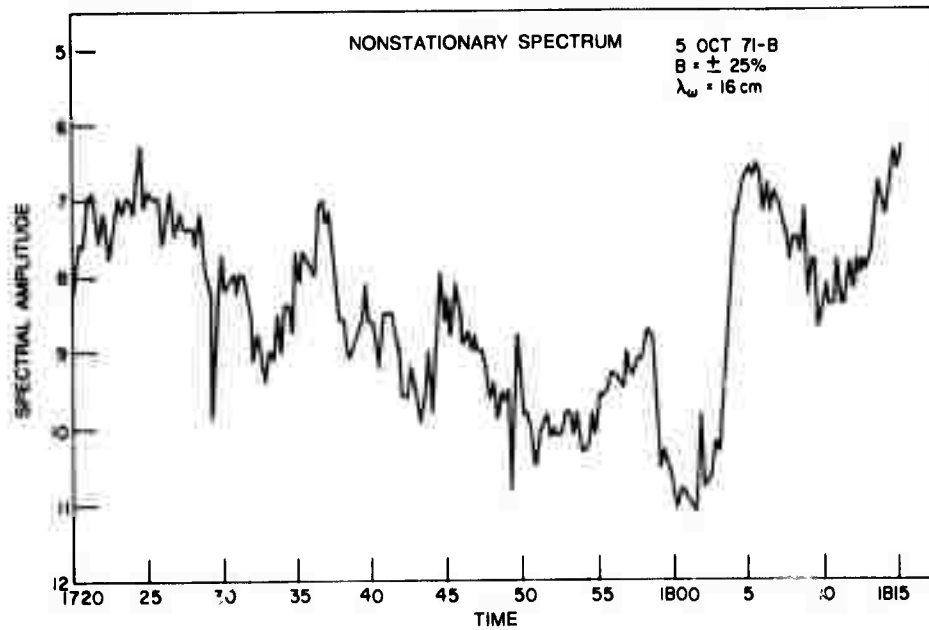


Figure 36

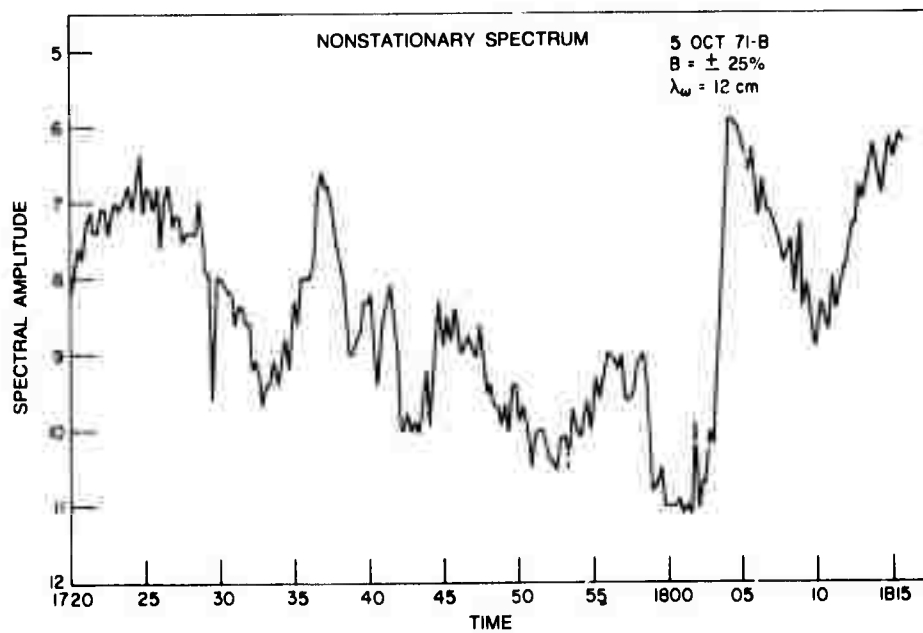


Figure 37

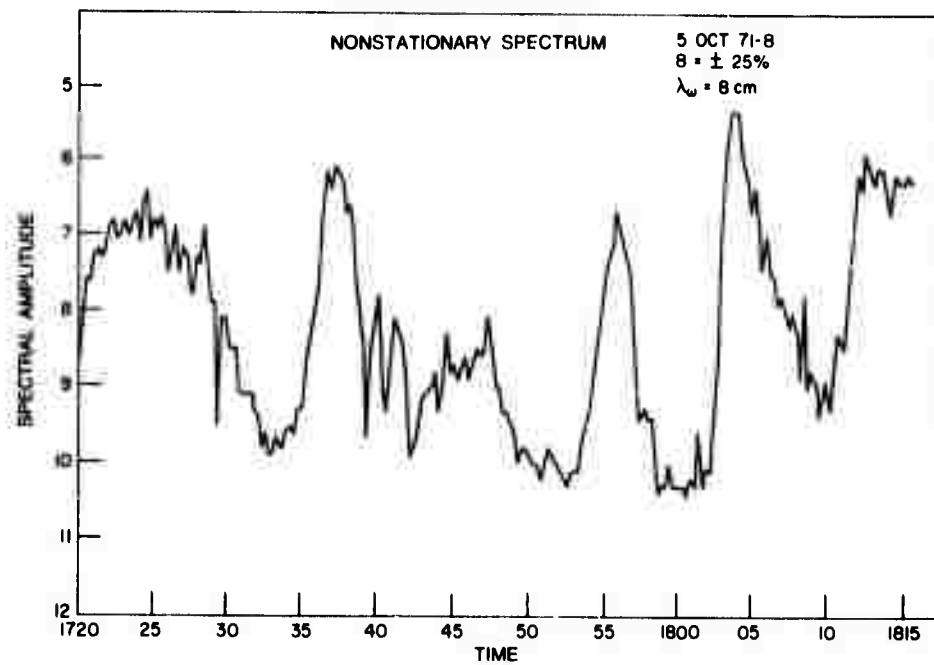


Figure 38

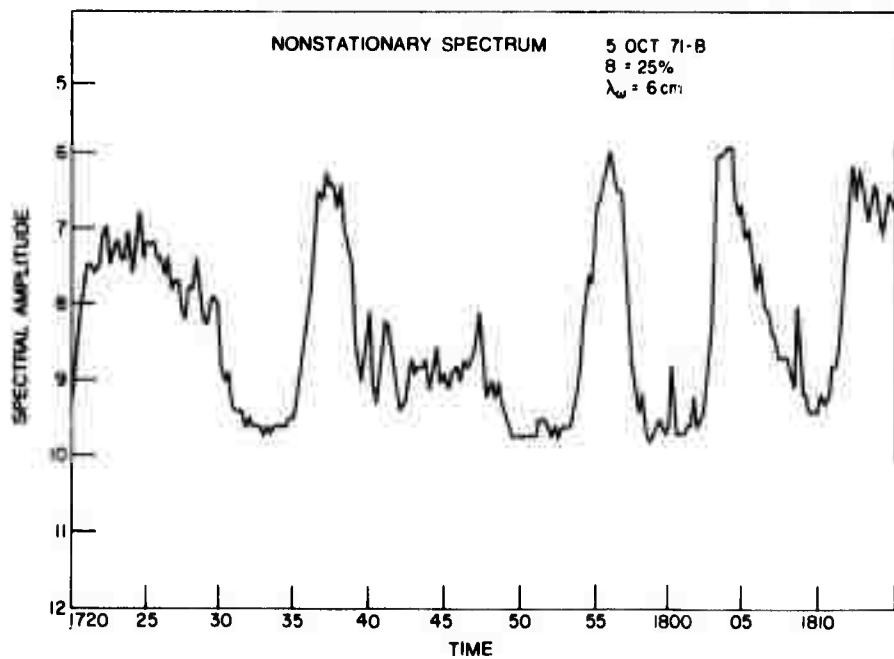


Figure 39

Figure 40 is a series of spectra for a short time interval about 1804 for Oct. 5. These data were obtained by recording each spectrum on film and obtaining the spectral amplitudes from microdensitometer recordings. The density recording was averaged in frequency space to obtain smoothing. The wind had been fairly near zero for a short time just prior to the first spectrum. In fact, the 1801:45 GMT plot showed no peak at the short wavelengths, just the rise at the low frequencies. Starting at the spectra plotted, it can be seen that the spectrum grows very rapidly, initially at the highest frequencies and spreading to the lower ones as time progresses. The curves show amplitudes during the initial stages of growth in excess of the dashed line drawn on each of the curves. Later, after equilibrium has been approached, the spectrum falls and stays at the level indicated by the dashed line. From these curves it is obvious that the transient spectral response exhibits and overshoot mechanism. Such an effect might not be observable with a frequency analysis alone, however, i.e., a wave pole. It is possible that during the initial stages of wave growth, the spectral energy is restricted to a narrow range of angles and diffuses in angle with time until an equilibrium directivity is achieved. This would make overshoot an observable for directionally sensitive sensors but obscure the effect for devices which measure frequency spectra. Unfortunately, the data collected during this run are insufficient to provide a definitive answer. The importance of this effect on the phenomenology of internal wave interactions with surface waves cannot be minimized. If the spectral collapse/growth commonly observed in the narrow slick-like bands is a combination of wave-wave interaction and wave-growth mechanisms, the interpretation of the interaction mechanism will be quite complicated.

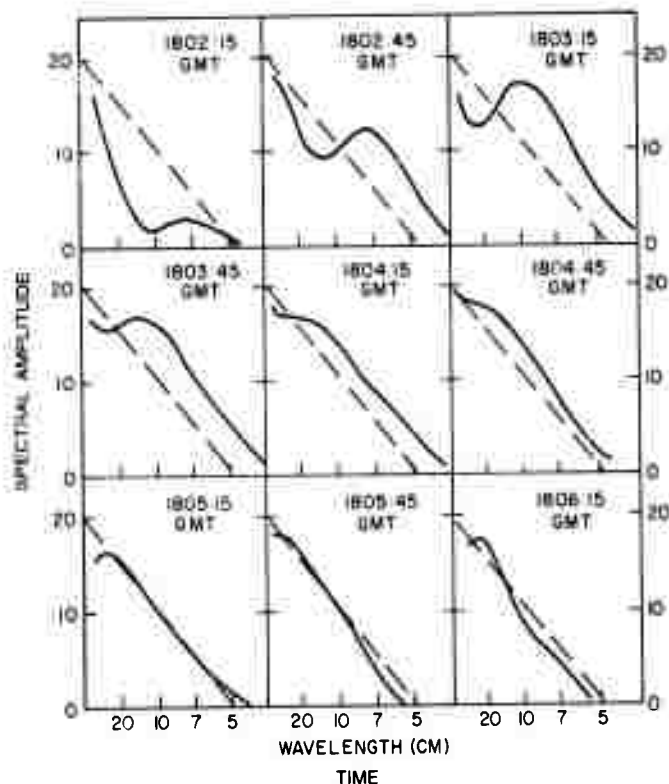


Fig. 40 — Temporal variation of the spectra of Oct. 5, 1971

Figures 41 through 47 show the spectral histories exhibited at the site during the time interval 2005 to 2052 on Oct. 5. The film for this run was placed at the 46-cm optical bench point, indicated as $L/2$; the spot size is 5.5 mm. The seven figures show a very rapid oscillation in spectral amplitude with a major dip at 2015 and subsequent dips at about 5-min intervals with diminishing intensity. This is mindful of a ringing effect after a transient and could be due to internal-wave patterns which have been observed from the thermistor-chain-array data. As the water wavelength analyzed approaches the shortest wavelength, the variation of the spectrum diminishes. This is probably due to a decrease in the recorded signal rather than a real effect. The small slopes recorded on film at these high spatial wavelengths are far enough down on the modulation transfer curve to exhibit low signal-to-noise ratios. It can be seen, however, that the effects attributed to swell or to packet distributions are still evident, though of smaller amplitude. This means that for film recording the signal levels at these wavelengths are quite small. In terms of the number of degrees of freedom contained in the sampled area, a data length of 5.5 mm and a film spatial frequency of about 20 lines/mm for the highest frequency of a wavelength of 3 cm, the measurement should be quite precise. The total number of degrees of freedom is about $5.5 \times 20 \times 20$ for the area. The conclusion here would be that better light sensitivity is needed to adequately record such short wavelengths.

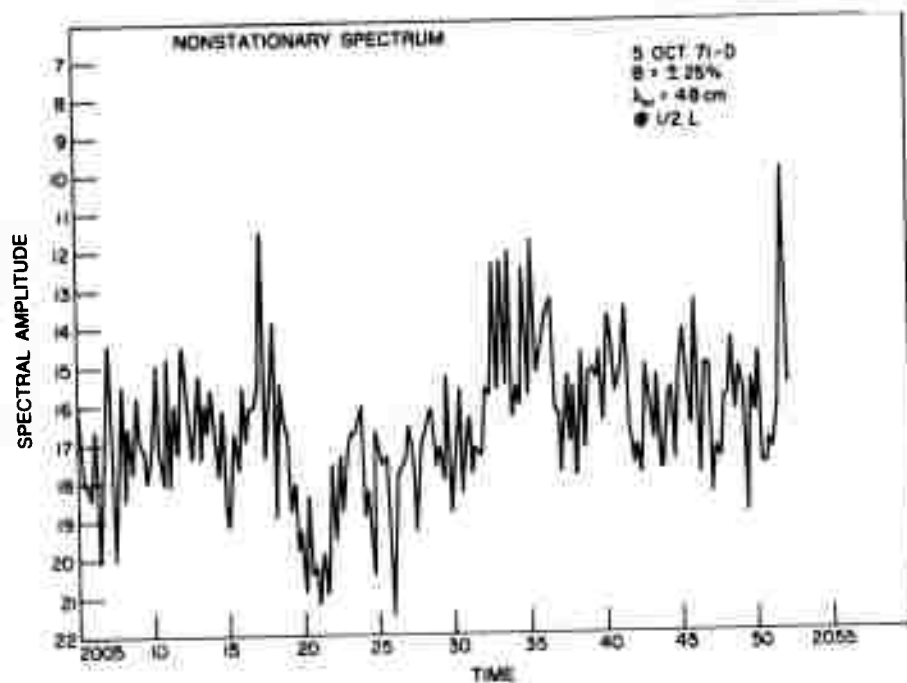


Figure 41

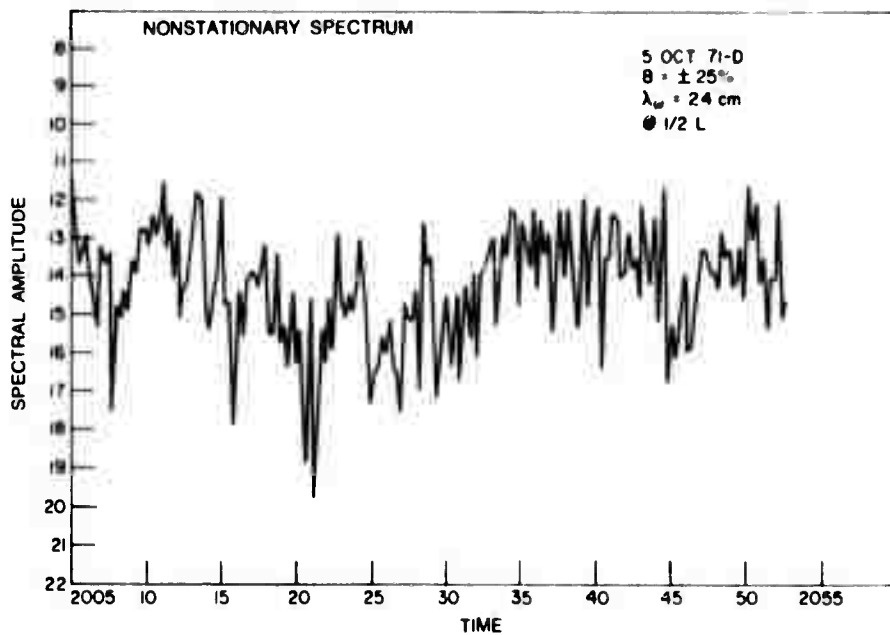


Figure 42

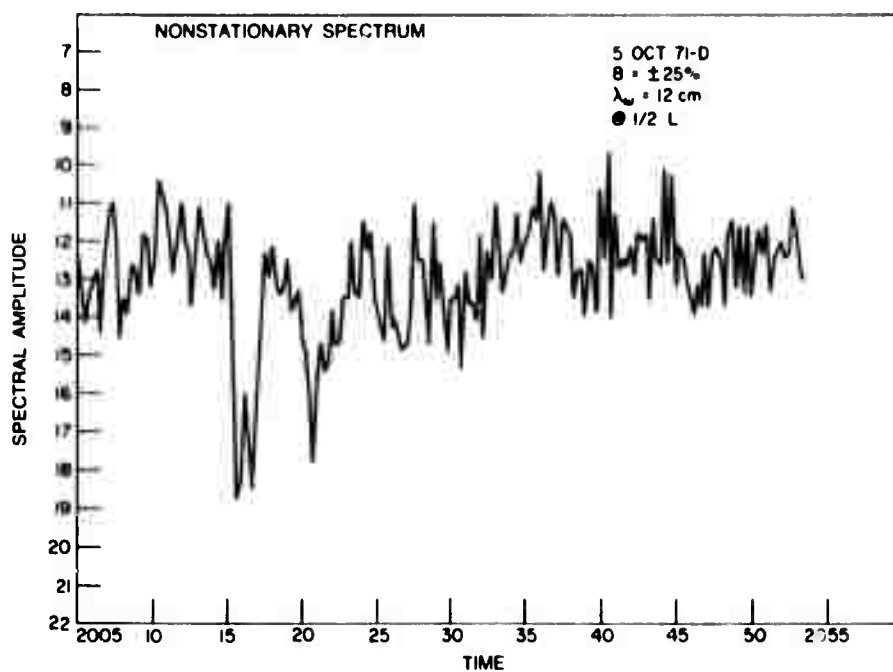


Figure 43

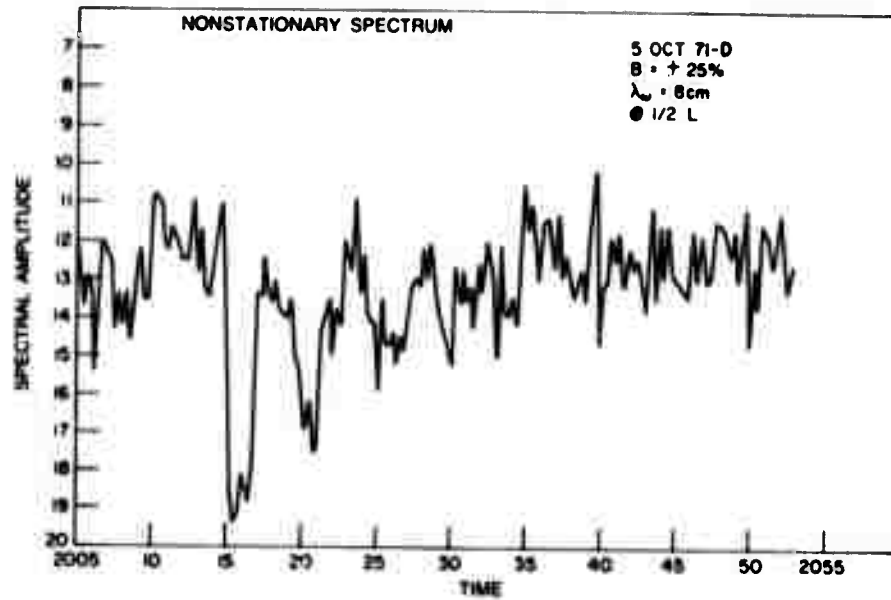


Figure 44

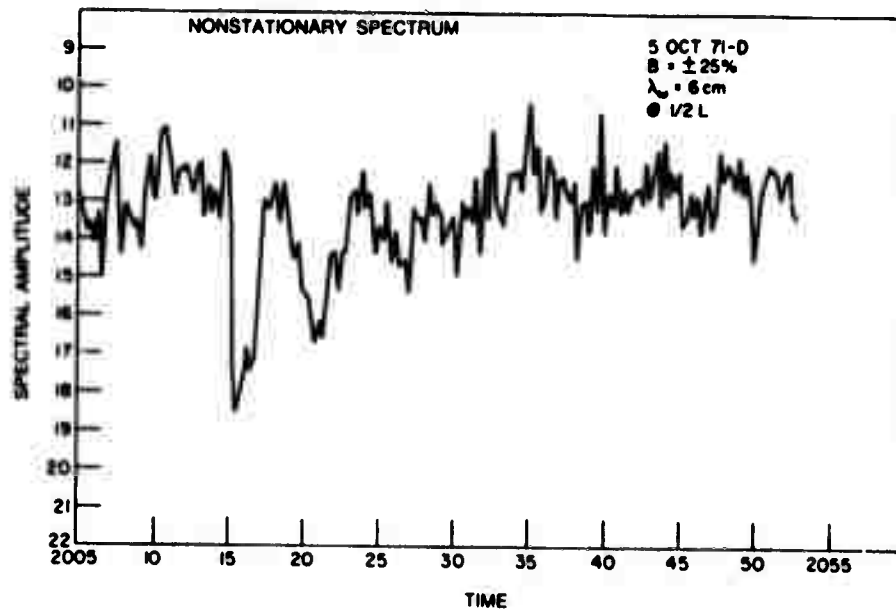


Figure 45

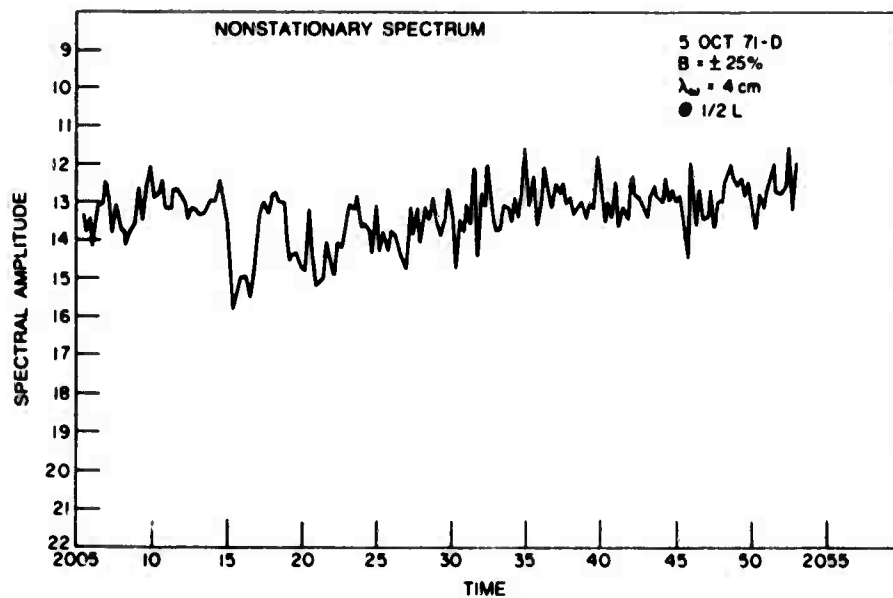


Figure 46

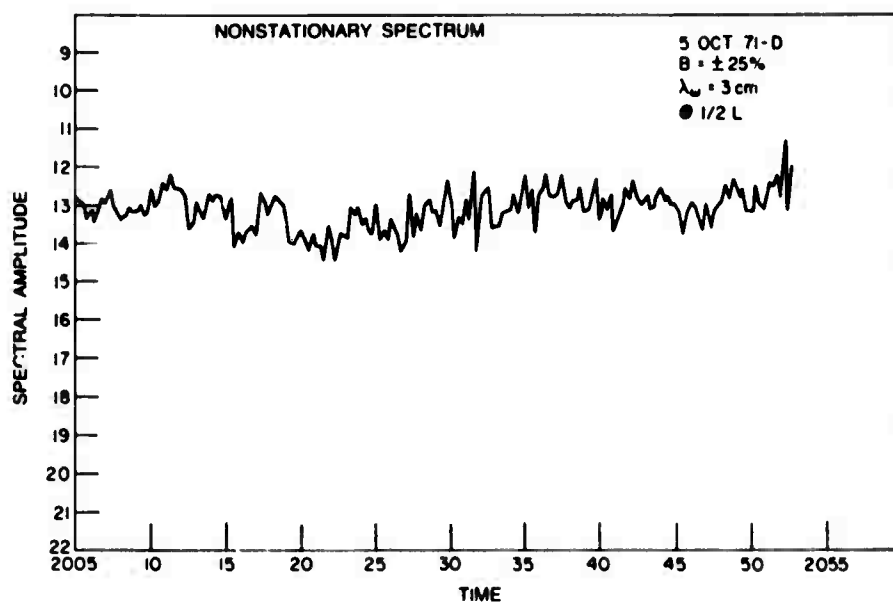


Figure 47

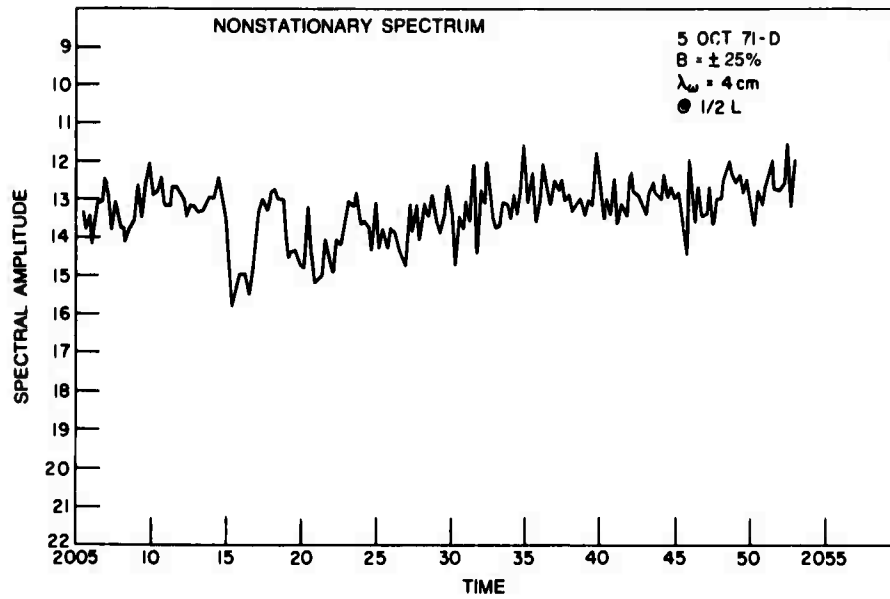


Figure 46

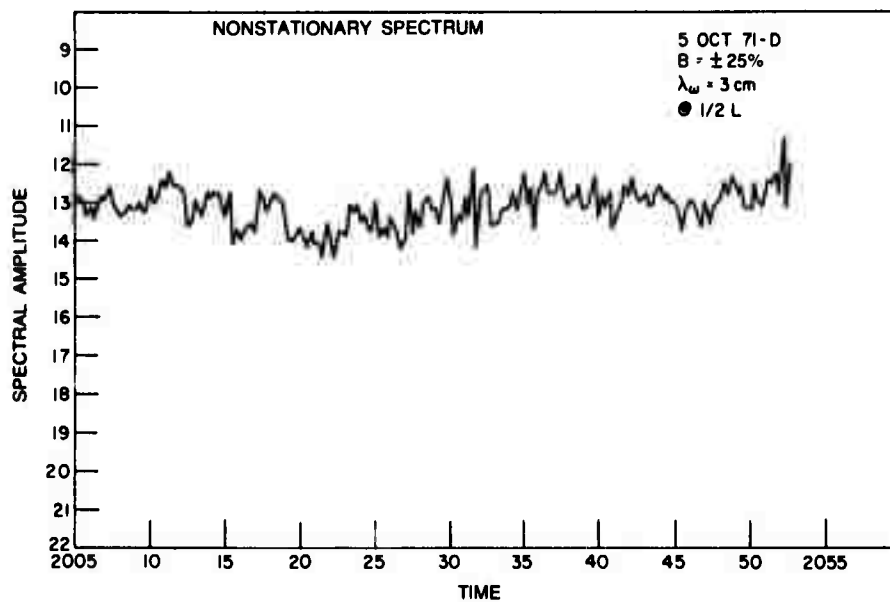


Figure 47

Figures 48 through 52 show another kind of effect. These data were taken on Oct. 6 between 1645 and 1722 GMT. There is but one strong event during this interval, that occurring about 1715. It is interesting, however, that the signature of the event changes with the wavelength analyzed. At the shortest wavelength, i.e., 6 cm, the event shows a major dip with a little overshoot following. At the longest wavelength there is no dip, but only a rise above the ambient level and a return to that level. Intermediate wavelengths show a progression from a dip to a rise tendency. This even again points out the complexity of the interaction being studied. Correlation with other sensors is a must if this run is to provide any quantitative information.

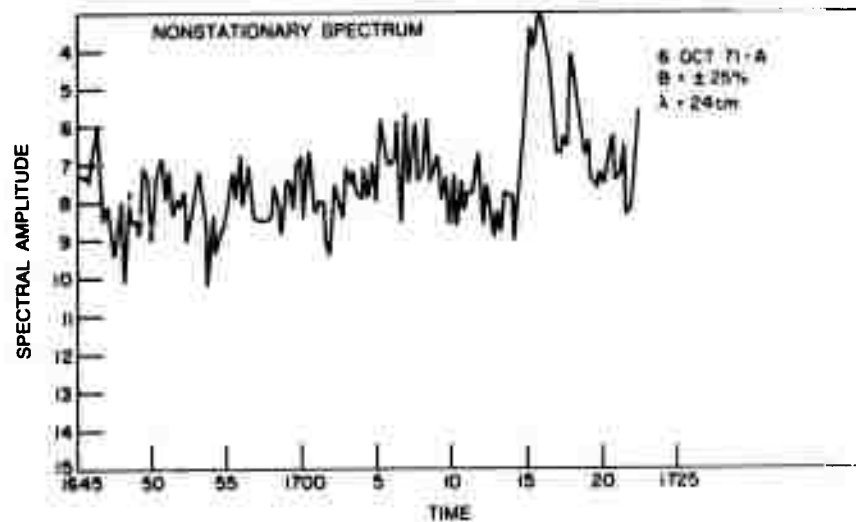


Figure 48

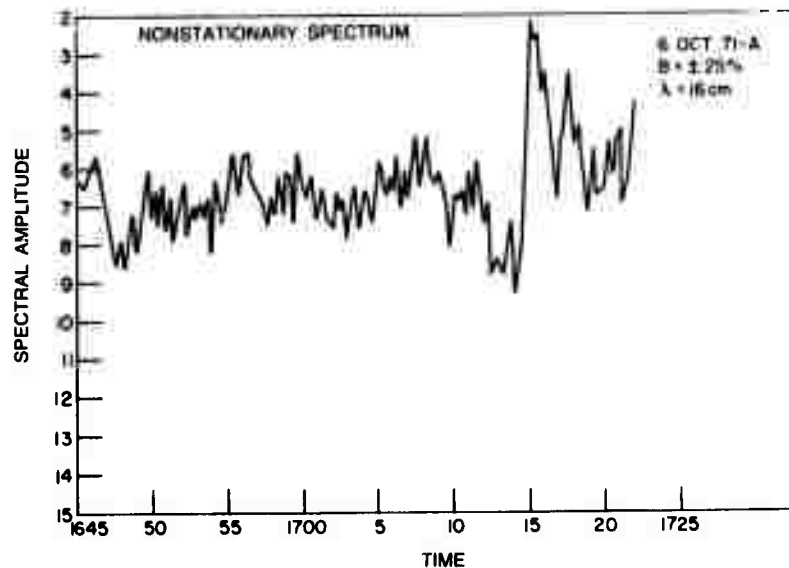


Figure 49

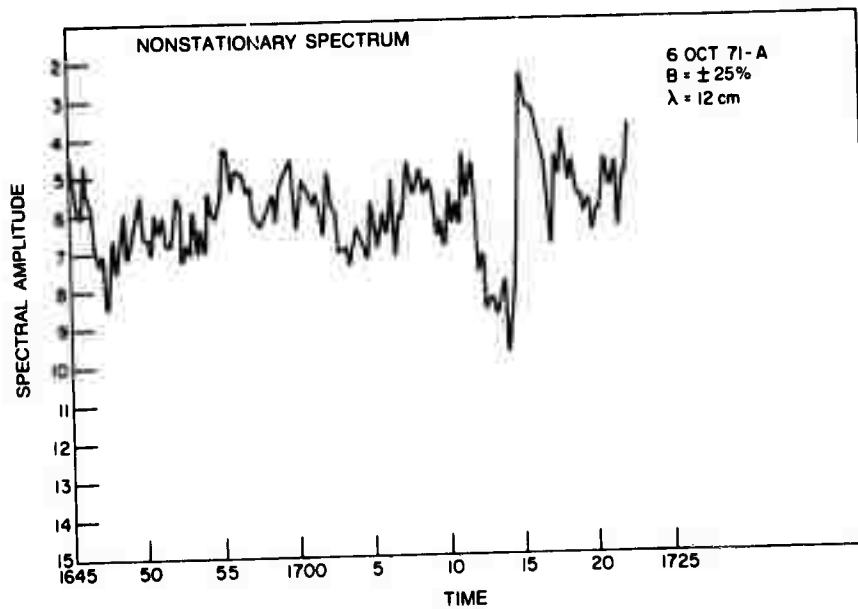


Figure 50

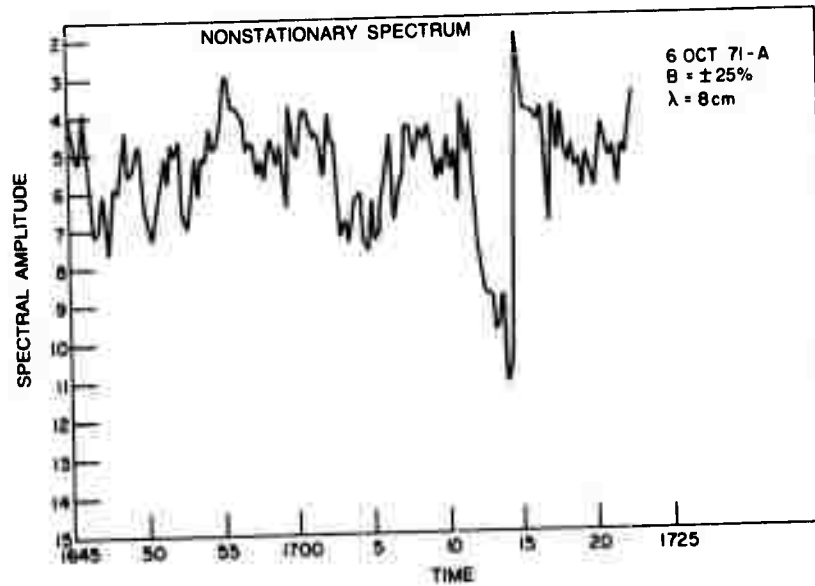


Figure 51

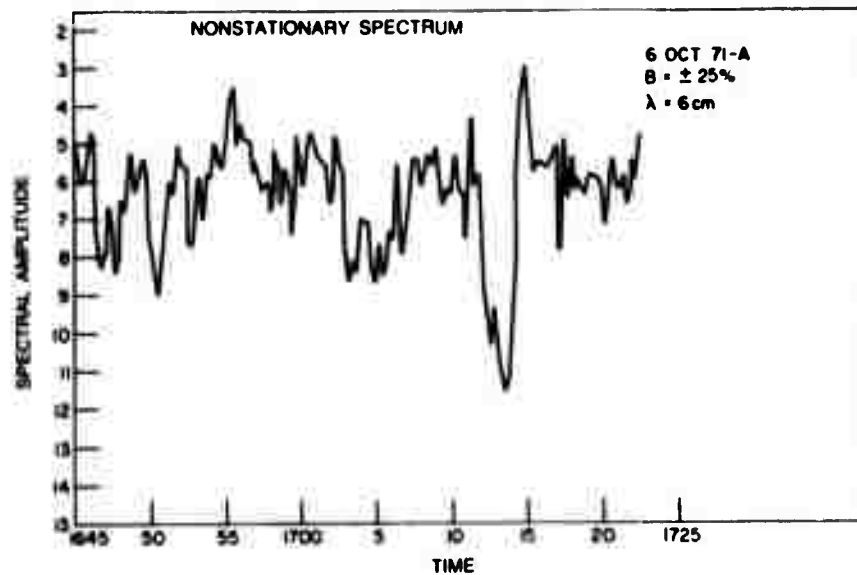


Figure 52

Figures 53 through 56 represent still another situation. This data was taken on Oct. 6 between 1855 and 1938 GMT. Here the fine structure is of large amplitude, and any internal-wave periodic modulation is buried in the noise. Drawing a smooth curve through the spectral histories does yield a small effect of perhaps ± 1 -dB modulation at a period of 6 to 7 min, buried in the swell fluctuation of ± 1.5 dB. An obvious interpretation of this situation is that the surface currents due to swell were larger than those due to the internal-wave system. Further, the wind level may have been sufficiently high to preclude the formation of biological slicks which might show the long-term coherence of the internal-wave system. Waveheight measurements and thermistor-chain records should be examined for this run to assess the validity of the above hypothesis.

Figures 57 through 63 show the spectrum at seven wavelengths for the hour 1607-1707 on Oct. 7. This run again shows the frequency dependence of the observed spectrum and how completely different patterns occur in different spectral regions. The longest wavelength shows a major event occurring at about 1642 in which only the level of the spectrum changes. At 24 cm, one can see large changes in the spectrum in the interval 1612 to 1637 GMT. The spectral signal varies by about 15 dB during that period. The 16-cm graph exhibits a behavior indicative of a pair of slicks, one at about 1620 and another at 1635. Here the signal between the slicks assumes a level of about 15 dB higher than in the slick. Again, as shorter wavelengths are approached, the entire level of the variability diminishes. This curve is perhaps the best evidence obtained for a frequency-dependent interaction of internal and wind waves. The signal at about 1632 differs drastically even in the range of 8 to 20 cm.

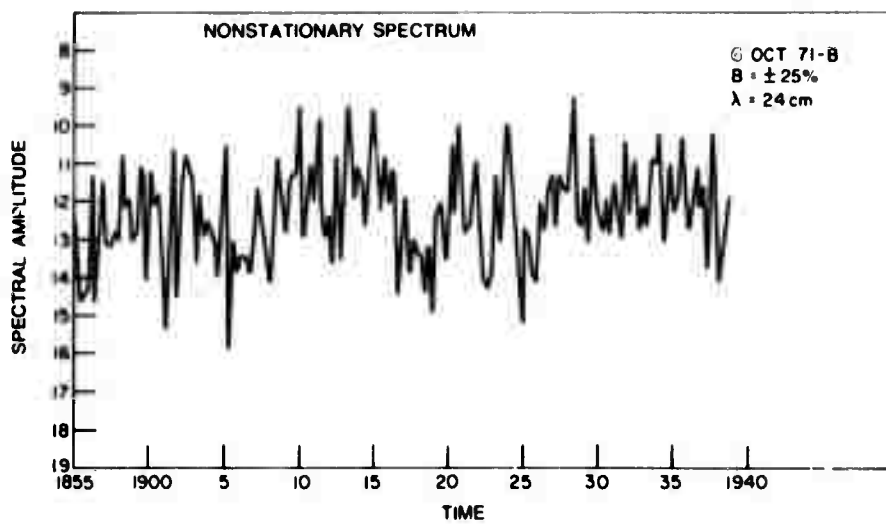


Figure 53

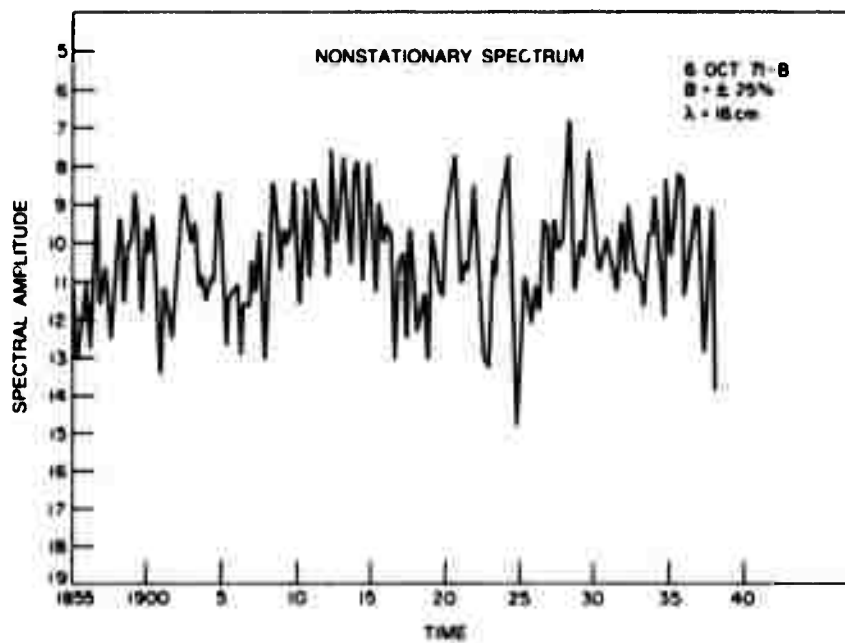


Figure 54

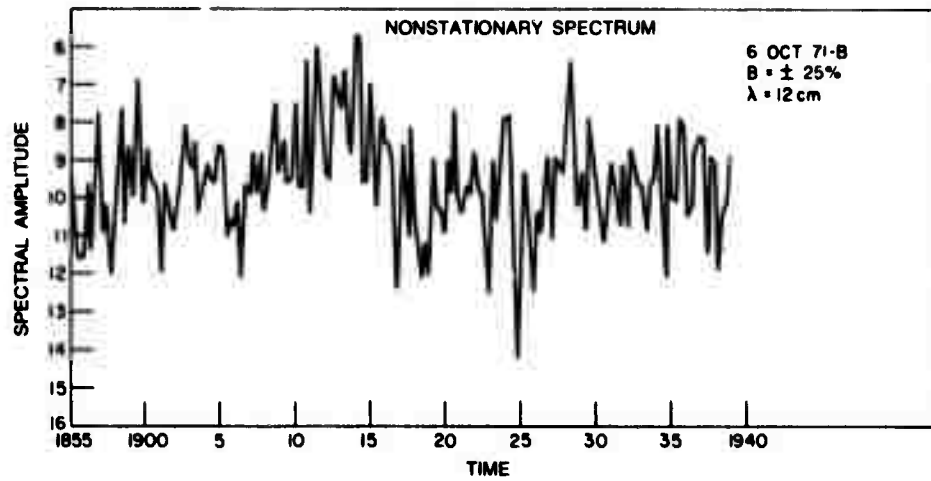


Figure 55

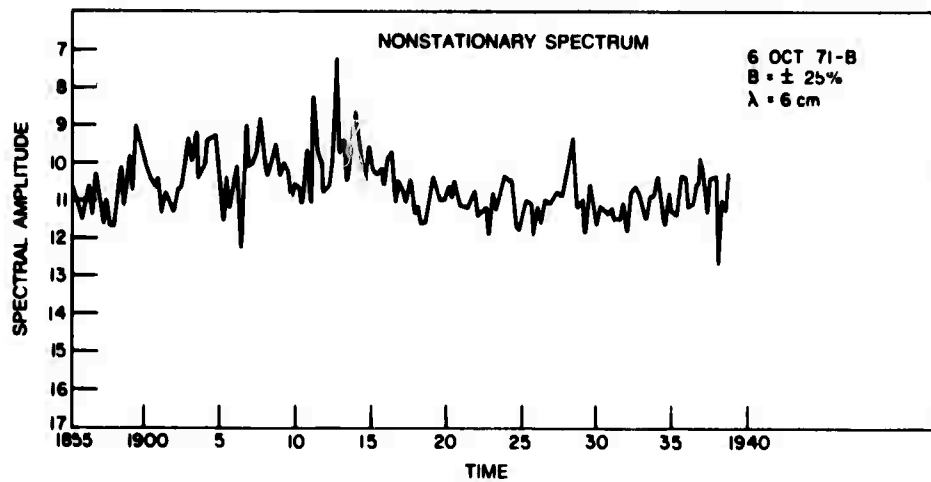


Figure 56

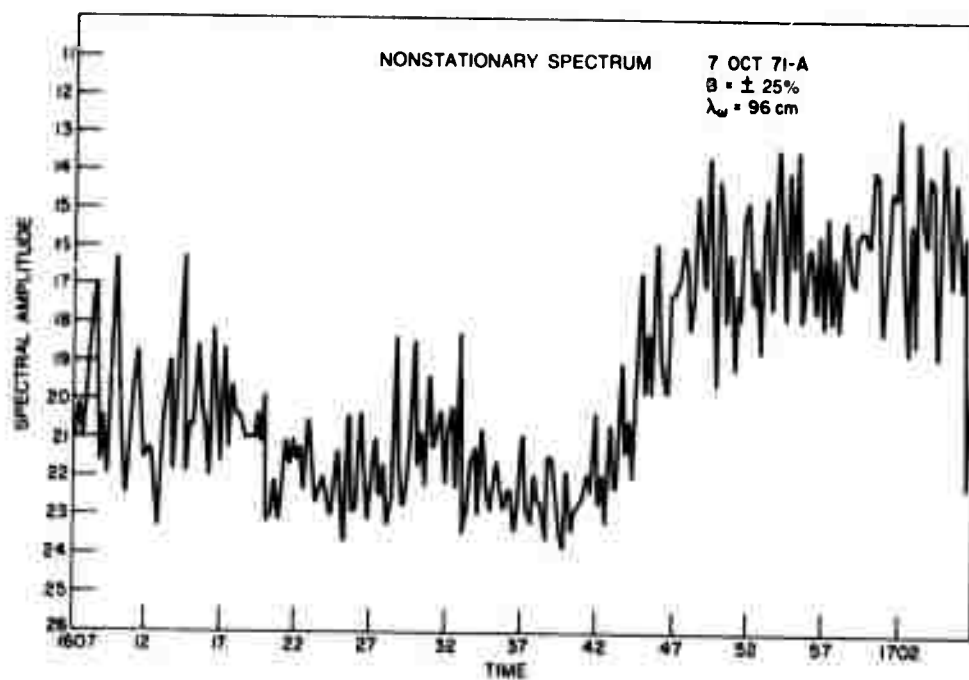


Figure 57

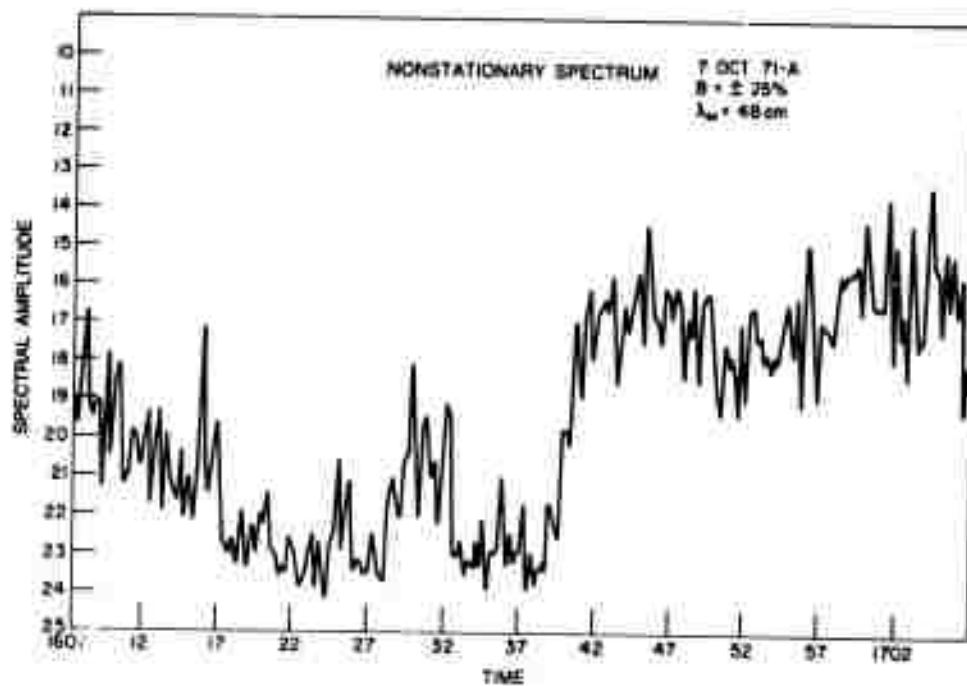


Figure 58

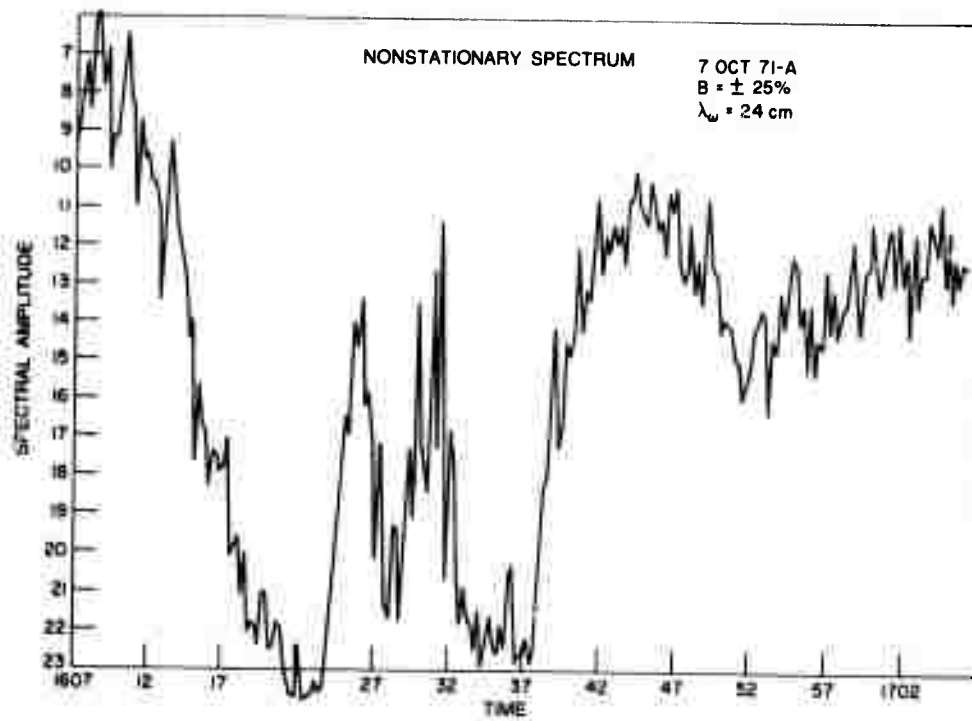


Figure 59

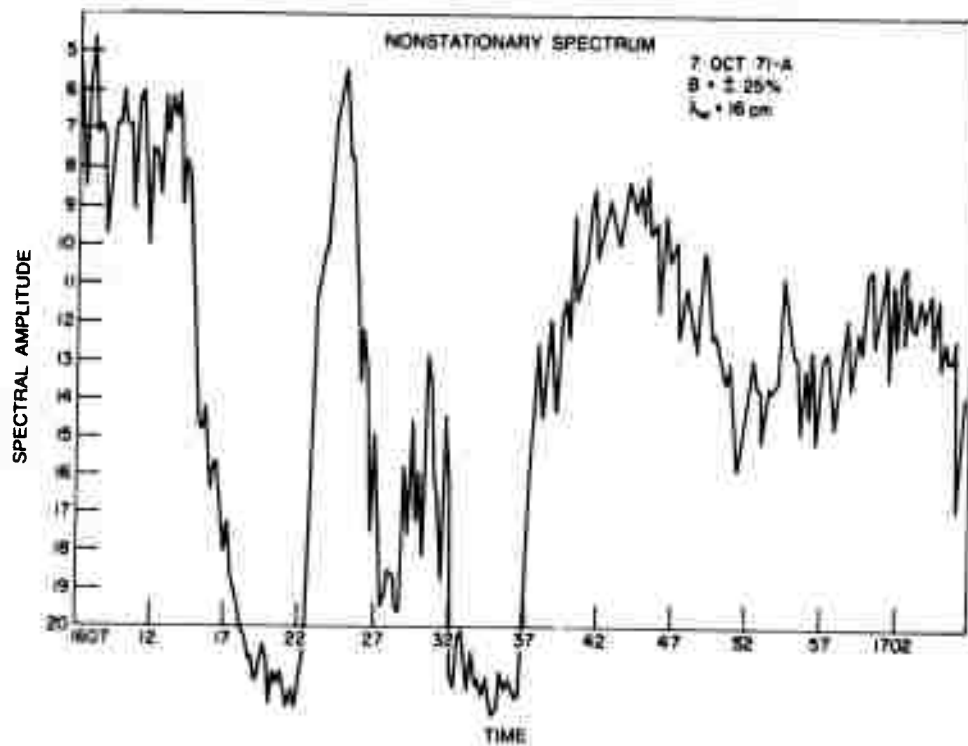


Figure 60

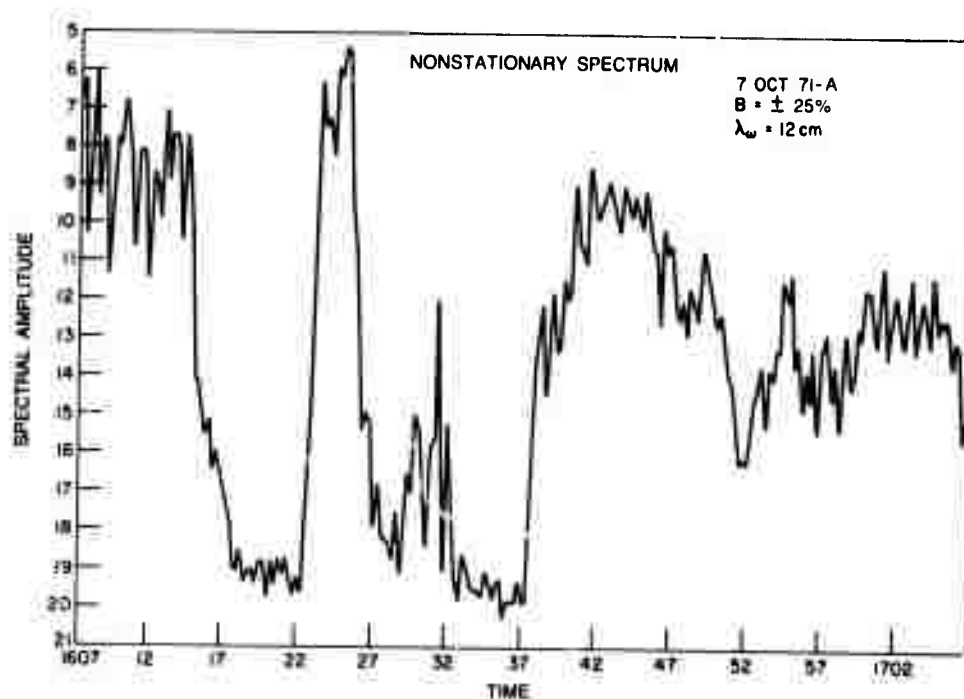


Figure 61

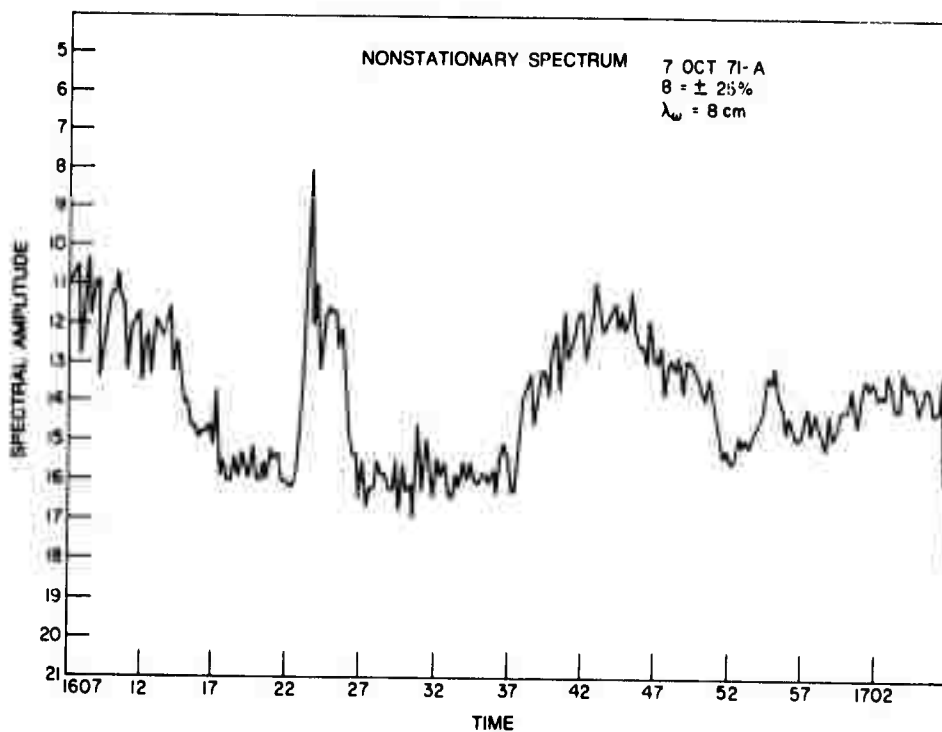


Figure 62

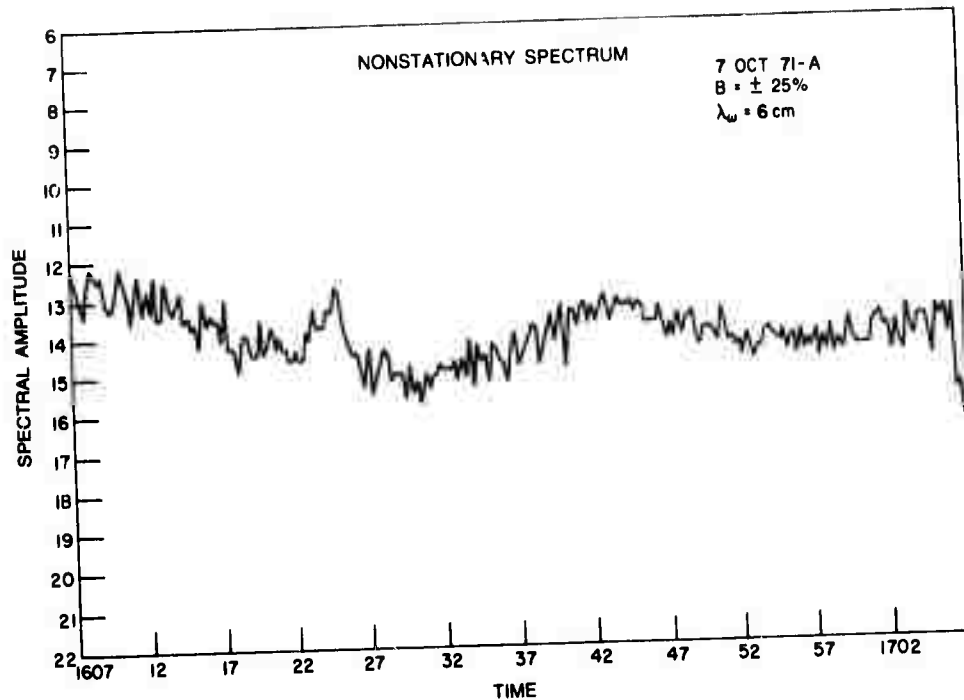


Figure 63

Figures 64 through 70 show the spectrum between 1727 and 1824 GMT on Oct. 7. This run is about the same as the preceding in both characteristics and interpretation. The analysis was performed in this case for $L/2$ in an attempt to obtain information at shorter wavelengths. In this case even the longest wavelength shows a slight dip at about 1747, but on proceeding to shorter wavelengths, another dip, which is even wider, begins to show up about 1730. In between, at about 1740, the spectrum rises about 8 dB above the lowest point. This might indicate the existence of two internal-wave crests separated by about 15 min in which the one occurring last has a sufficiently strong effect to alter the spectrum at 24 cm, whereas the preceding one had little or no effect at that wavelength. It is conceivable that the pair of slicks differed in their makeup; one may have had naturally occurring oils associated with it, making the attenuation of waves of a different bandwidth and magnitude than the other slick. After a long period of inactivity, one would expect the first wave to have the effect of sweeping the surface of material, leaving the interaction of the succeeding waves with a more pure current effect. The internal-wave situation at San Diego is sufficiently complex that crossed waves could transfer material from one internal-wave system to another, depending on the relative strength and period of the waves. This data may therefore be of value in assessing the distinction between chemical and nonchemical slicks. Other sensors will have to be used to unravel the questions raised by this run.

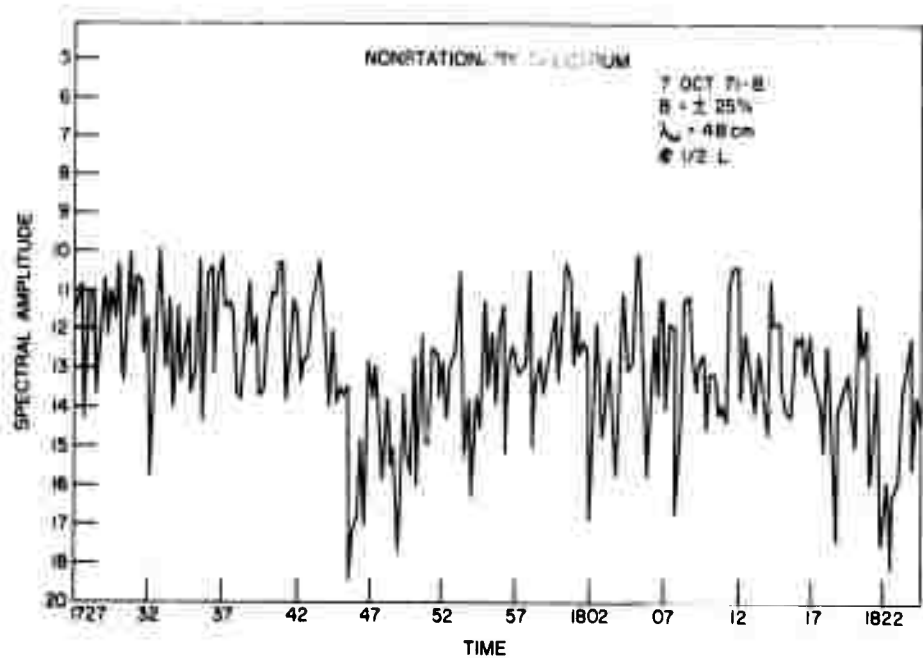


Figure 64

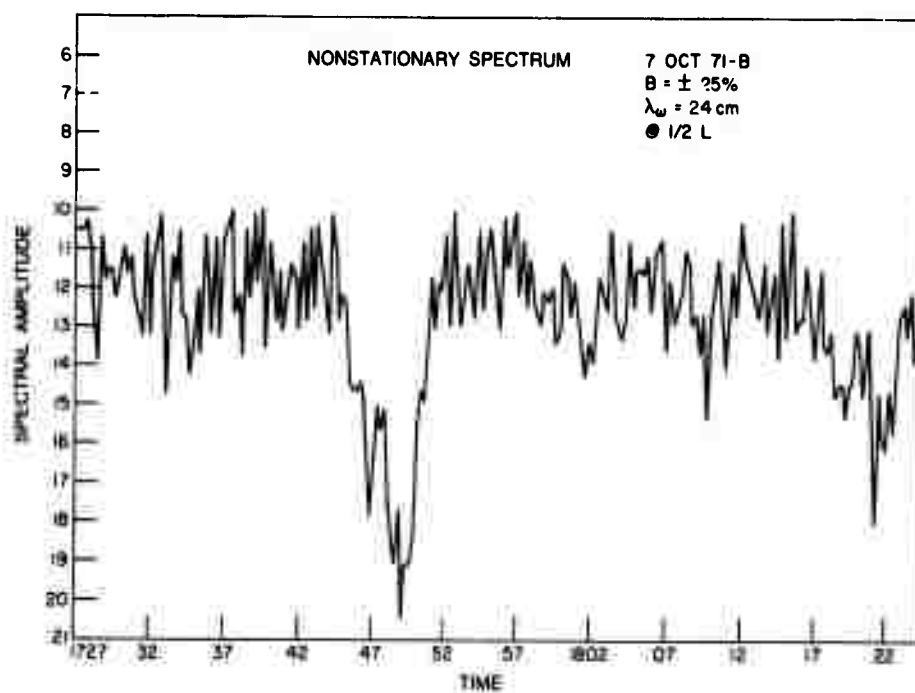


Figure 65

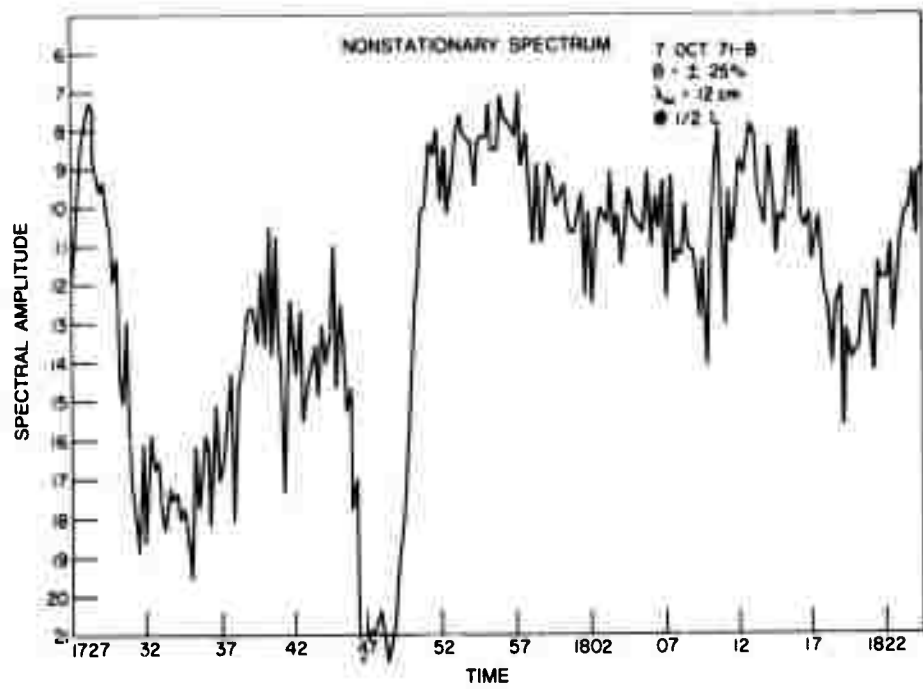


Figure 66

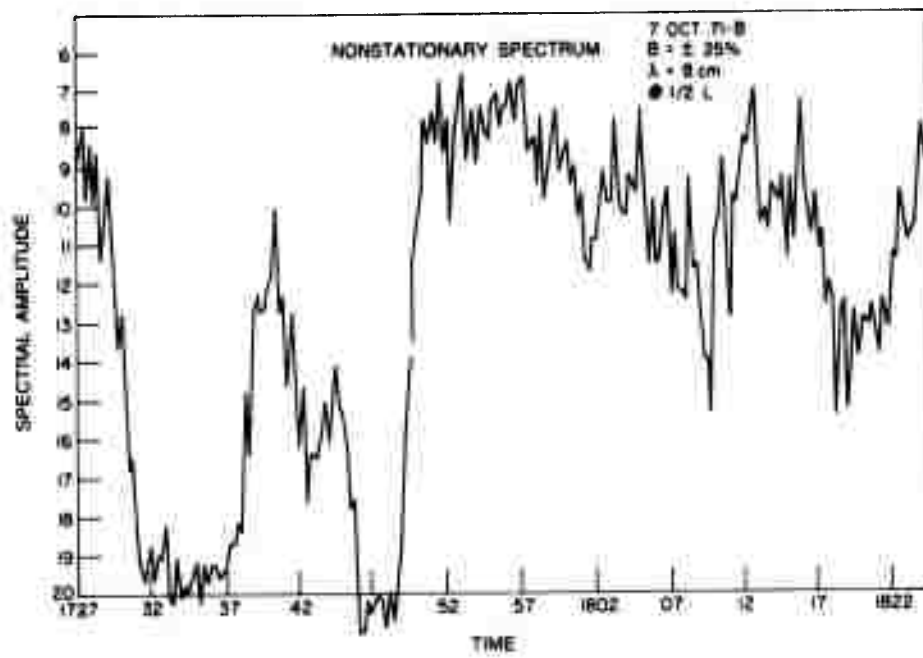


Figure 67

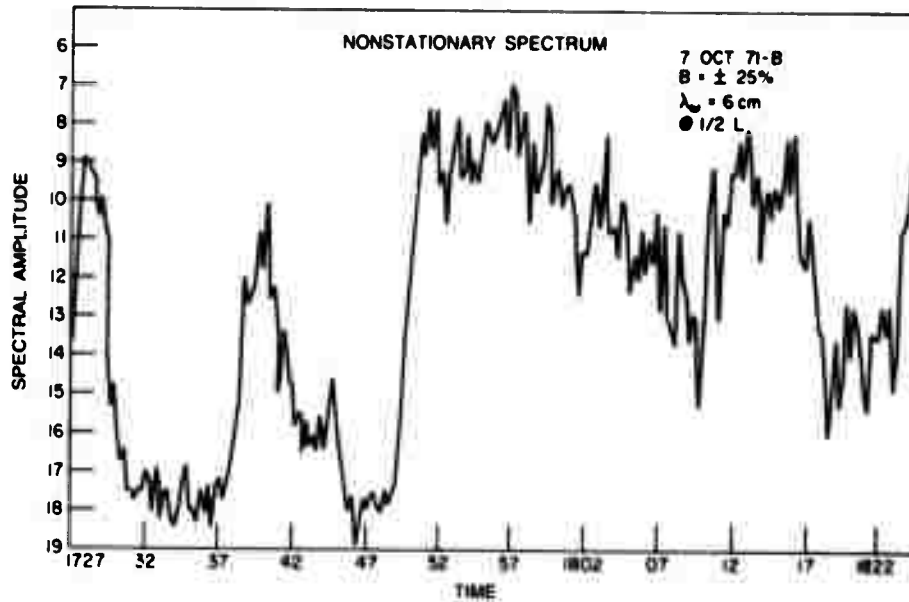


Figure 68

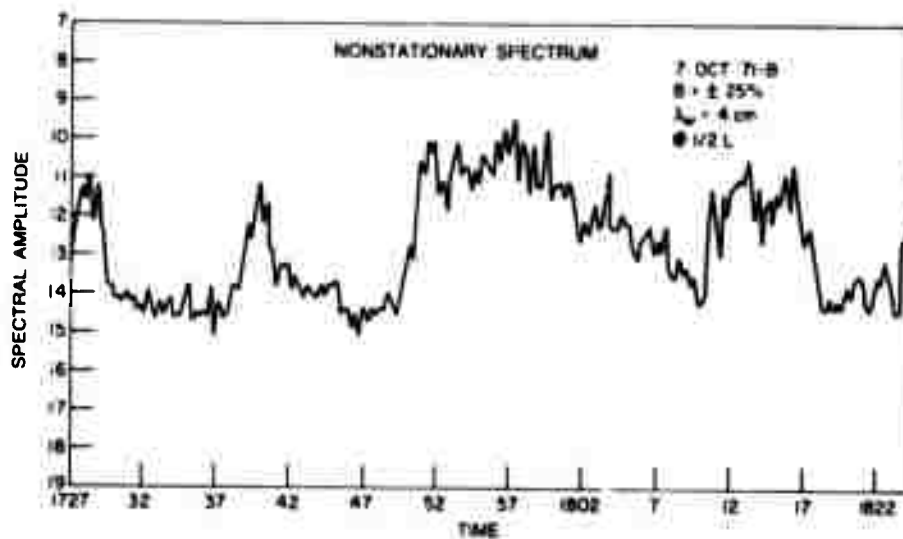


Figure 69

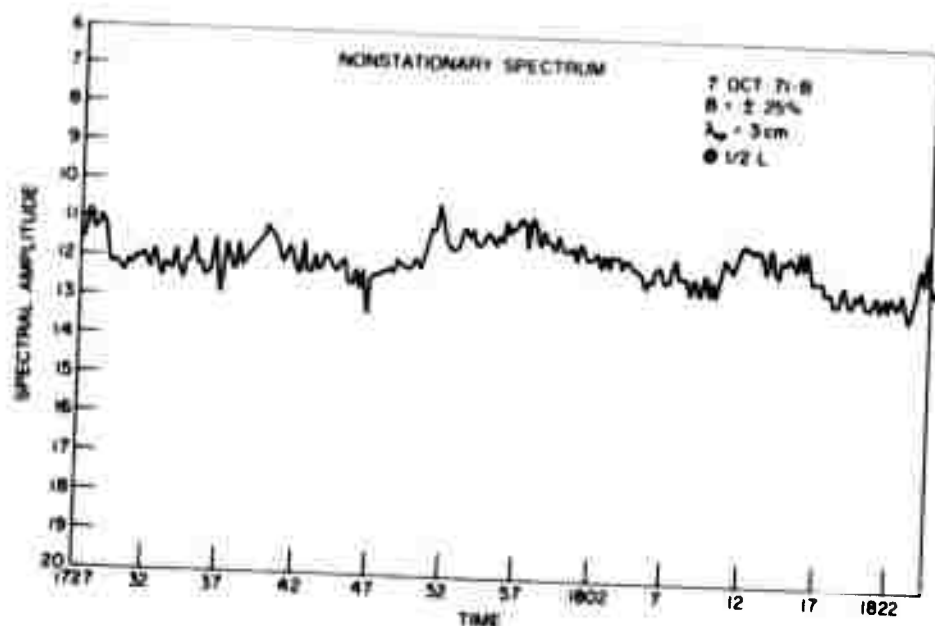


Figure 70

CONCLUSIONS

The optical measurements performed at the NURDC tower in San Diego during the summer of 1971 were highly successful. A heretofore impossibly huge amount of directional data was obtained and analyzed in the study of the interaction of internal waves and surface waves. More than 2000 spectra were generated to investigate the frequency dependence of this interaction. The results point out a few highly interesting features of the process which at this juncture are not explicable.

During the eleven runs, a wide range of conditions was experienced. The result is that each run seems to exhibit at least a slightly different pattern. It appears that a significantly greater body of data would need to be analyzed and correlated with sensors of other parameters to determine the physics of the interaction process. The observed situation consists of a wave-generation mechanism, spectral inhomogeneity (packets), body currents, surface currents, wind magnitude, wind direction, surface contaminants, temperature effects, and many other independent parameters. Some insight into the physics of the interaction is available from the optical data. From the optical data alone, it can be determined that the interaction effects are far from small; in fact, nonstationary spectral fluctuations of up to 15 dB have been recorded. Further, there is evidence that surface-wave modulation effects of about 1 dB are measurable even with ocean swell perturbations exceeding 1 dB. It should be expected that the experience gained in this program could lead to a more sophisticated measurement-and-analysis program to delineate with more certainty the fundamental principles involved in this interaction.

REFERENCES

1. J. W. Goodman, *Introduction to Fourier Optics*, McGraw Hill, San Francisco, 1968.
2. B. Kinsman, *Wind Waves*, Prentice-Hall, Inc., Englewood Cliff, 1965.
3. L. Moskowitz and W. J. Pierson, Jr., "A Proposed Spectral Form for Fully Developed Wind Seas Based on the Similarity Theory of S. A. Kitaigorodskii," *J. Geophys. Res.* No. 24, 5181 (1964).
4. D. Stilwell, Jr., "Directional Energy Spectra of the Sea from Photographs," *J. Geophys. Res.* 74, No. 8, 1974 (1969).